

A framework for evaluating ocean mixed layer depth evolution

Alexandre Legay¹, Bruno Deremble², Thierry Penduff³, Pierre Brasseur⁴, and Jean-Marc Molines⁴

¹Institut des Géosciences de l'Environnement

²Université Grenoble Alpes

³Laboratoire de Glaciologie et Géophysique de l'Environnement, CNRS

⁴French National Centre for Scientific Research (CNRS)

January 16, 2024

A framework for evaluating ocean mixed layer depth evolution

Alexandre Legay¹, Bruno Deremble¹, Thierry Penduff¹, Pierre Brasseur¹,
Jean-Marc Molines¹

¹Univ. Grenoble Alpes, CNRS, INRAE, IRD, Grenoble INP, IGE, 38000 Grenoble, France

Key Points:

- A parameter space is proposed to assess the evolution of the mixed layer depth for realistic forcings and preconditioning conditions
- The predictive skill of the parameter space is evaluated with a collection of 1D simulations
- Two applications demonstrate the utility of the parameter space, when used with realistic 3D ocean simulations

Corresponding author: Alexandre Legay, alexandre.legay@univ-grenoble-alpes.fr

13 **Abstract**

14 The mixed layer plays a crucial role as an entry or exit point for heat, salt, momen-
 15 tum, and nutrients from the surface to the deep ocean. In this study, we introduce a frame-
 16 work to assess the evolution of the mixed layer depth (MLD) for realistic forcings and
 17 preconditioning conditions. Our approach involves a physically-based parameter space
 18 defined by three dimensionless numbers: λ_s representing the relative contribution of the
 19 buoyancy flux and the wind stress at the air-sea interface, R_h the Richardson number
 20 which characterizes the stability of the water column relative to the wind shear, and f/N_h
 21 which characterizes the importance of the Earth’s rotation (ratio of the Coriolis frequency
 22 f and the pycnocline stratification N_h). Four MLD evolution regimes (“restratification”,
 23 “stable”, “deepening” and “strong deepening”) are defined based on the values of the
 24 normalized temporal evolution of the MLD. We evaluate the 3D parameter space in the
 25 context of 1D simulations and we find that considering only the two dimensions (λ_s , R_h)
 26 is the best choice of 2D projection of this 3D parameter space. We then focus on this
 27 two-dimensional λ_s - R_h parameter space and we present how this framework can be used
 28 to analyze 3D realistic ocean simulations. We discuss the impact of the horizontal res-
 29 olution (1° , $1/12^\circ$, or $1/60^\circ$) and the Gent-McWilliams parameterization on MLD evo-
 30 lution regimes.

31 **Plain Language Summary**

32 Vertical mixing of water in the ocean occurs when cold air temperatures create dense
 33 cold water at the surface that tends to sink in the ocean or when a strong wind induces
 34 turbulence at the ocean surface. These processes mix heat and salt and create a layer
 35 at the top of the ocean that has a uniform temperature and salinity and that is called
 36 the “mixed layer”. This mixed layer plays a fundamental role in the Earth climate sys-
 37 tem, and the representation of its evolution in ocean models hence needs to be assessed.
 38 For this purpose, we propose to map the mixed layer evolution in a three-dimensional
 39 space where the first axis is related to the wind and the surface heat flux, the second axis
 40 to the stability of the water column, and the third axis to the Earth’s rotation. We show
 41 that this tool performs well statistically and we present how to use it in the context of
 42 realistic ocean models.

1 Introduction

The evolution of the mixed layer near the air-sea interface is primarily driven by the vertical mixing and restratification processes. Vertical mixing is usually driven by winds, surface cooling, brine rejection, Langmuir turbulence, and wave breaking (Marshall & Schott, 1999; Q. Li et al., 2019; Vreugdenhil & Gayen, 2021). In contrast, restratification processes are driven by solar heating, freshwater flux, or lateral processes such as mixed layer instabilities (see for example Boccaletti et al., 2007; Fox-Kemper et al., 2007). Accurately representing the mixed layer depth (MLD) evolution is crucial for capturing many physical and biogeochemical mechanisms, such as the sequestration of heat and carbon by the ocean (e.g. Banks & Gregory, 2006; Bernardello et al., 2014), the dynamics of marine ecosystems (e.g. Sverdrup, 1953; Lévy et al., 1998; Taylor & Ferrari, 2011), and the representation of the Atlantic meridional overturning circulation (e.g. Kuhlbrodt et al., 2007).

Historically, various approaches have been proposed to describe the evolution of the MLD which can be categorized into three main categories: bulk mixed layer models, similarity models, and turbulence closure models. For bulk mixed layer models, the governing equations of fluid dynamics are integrated over the mixed layer and represent the evolution of integrated properties (e.g. Kraus & Turner, 1967; Pollard et al., 1973; Price et al., 1986; Gaspar, 1988). These models have been used to derive theoretical scalings for the evolution of the MLD, such as the wind-driven deepening $h \propto u_* N^{-1/2} t^{1/2}$ (Pollard et al., 1973), observed empirically by Price (1979), and the free convection scaling $h \propto Q^{1/2} N^{-1} t^{1/2}$ (Turner, 1973; Van Roekel et al., 2018) measured empirically by Souza et al. (2020) (h being the MLD, u_* the surface friction velocity, t the time, Q the net surface heat flux and N the Brunt Väisälä frequency).

The second class of models are the similarity models such as the K-Profile Parameterization (KPP, Large et al., 1994) or the OSMOSIS model (Damerell et al., 2020; Madec et al., 2022). These models assume that the vertical profiles of tracers and momentum are self-similar. With this self-similarity hypothesis, turbulent fluxes can be computed by scaling a predefined profile shape with the magnitude of the surface forcing. Although the KPP model successfully captures many observed features of the ocean's boundary layer, it relies on empirical relationships and is not derived from first principles. Nev-

74 ertheless, KPP remains one of the most widely used parameterizations of convection in
 75 ocean models (Van Roekel et al., 2018; Q. Li et al., 2019; Souza et al., 2020).

76 The last class of models consists of the turbulence closure models. These models
 77 consider equations of higher order moments of the turbulent quantities and make some
 78 assumptions about their formulations in order to close the problem (e.g. Mellor, 1973;
 79 Mellor & Yamada, 1974, 1982). Widely used models in this class include the Turbulent
 80 Kinetic Energy (TKE) models, which solve a prognostic equation for TKE (Gaspar et
 81 al., 1990), and the Generic Length Scale (GLS) models which include an additional prog-
 82 nostic equation for the mixing length l (global description: Umlauf and Burchard (2003,
 83 2005); examples of models of this type: $k-\epsilon$: Hanjalić and Launder (1972); Rodi (1987),
 84 $k-kl$: Mellor and Yamada (1982), $k-\omega$: Wilcox (1988), $k-\tau$: Zeierman and Wolf-
 85 shtein (1986); Thangam et al. (1992)). Some models do not fit into one of the three afore-
 86 mentioned classes, such as the energetics-based Planetary Boundary Layer scheme (ePBL,
 87 Reichl & Hallberg, 2018), which combines a depth-dependent bulk mixed layer model
 88 with a turbulence closure model.

89 Currently, most climate simulations either use TKE or KPP models for vertical mix-
 90 ing (Zhu et al., 2020). The MLD evolution of these climate simulations depends on (i)
 91 the choice of vertical mixing scheme, (ii) the impact of resolved lateral processes, and
 92 (iii) as parameterizations for unresolved lateral effects (e.g. the Fox-Kemper et al. (2007)
 93 and the Gent and McWilliams (1990) parameterizations). Consequently, objectively com-
 94 paring the MLD evolution in these climate simulations is challenging (Treguier et al.,
 95 2023). Common approaches involve comparing hydrographic sections at specific loca-
 96 tions (e.g. evaluation at the Papa station: Gaspar et al., 1990; Large et al., 1994; Bur-
 97 chard & Bolding, 2001; Giordani et al., 2020), and/or conducting intercomparisons at
 98 specific times (e.g. with intercomparisons of MLD maps: Gutjahr et al., 2021; Heuzé,
 99 2017), and/or using indirect metrics of the MLD evolution (e.g. by comparing the amount
 100 of deep water formed: Koenigk et al., 2021). However, these approaches only explore a
 101 limited range of forcings and preconditioning conditions.

102 In this paper, we adopt a more comprehensive approach by considering all possi-
 103 ble ranges of forcings and preconditioning conditions in a suitable parameter space. Belcher
 104 et al. (2012) and Q. Li et al. (2019) have pioneered this approach to evaluate the rep-
 105 resentation of Langmuir circulation in different vertical mixing schemes. They proposed

106 a two-dimensional parameter space, with the first dimension (*i.e.* the first dimension-
107 less number) assessing the relative importance of the wind and the wave forcings, and
108 the second dimension characterizing the relative importance of wave and buoyancy forc-
109 ings. In this parameter space, Belcher et al. (2012) and Q. Li et al. (2019) defined the-
110 oretical boundaries to highlight the importance of different surface forcings. Subsequently,
111 Large eddy simulations (LES) carried out in the literature were placed in this param-
112 eter space to see which regimes are explored by these simulations. Their objective was
113 to identify a potential bias arising from miscalibration of the LES simulations used to
114 establish parameterizations.

115 Following the approach of Q. Li et al. (2019), our objective is to propose a dedi-
116 cated parameter space to describe the evolution of the MLD. This parameter space aims
117 to capture the MLD evolution dependency on the relative importance of wind and buoy-
118 ancy forcings, preconditioning conditions (Marshall & Schott, 1999), and the influence
119 of Earth’s rotation. More precisely, we will evaluate the relative deepening or shoaling
120 of the MLD over a 1-day period ($\partial_t h/h$ from noon to noon expressed in %/day). To keep
121 the practicability of having few parameters, we have decided to exclude several processes
122 (such as waves). Our study demonstrates that, at first order, three dimensionless num-
123 bers are enough for characterizing MLD evolution. In contrast to Q. Li et al. (2019), our
124 approach involves directly plotting the values of MLD evolution $\partial_t h/h$ in the param-
125 eter space. This direct visualization allows for a more straightforward comparison of the
126 behavior of different simulations.

127 This article is constructed as follows. First, we present in section 2 the three di-
128 mensionless numbers that constitute the parameter space. Secondly, we show in section
129 3.1 that MLD evolution regimes naturally emerge in this parameter space in the con-
130 text of 1D simulations. Thirdly, we present in section 3.2 and section 3.3 two applica-
131 tions for showing how the parameter space can be used in practice with 3D realistic ocean
132 models. The first application is about the impact of the lateral resolution on the MLD
133 evolution regimes. The second one focuses on the effect of the Gent McWilliams param-
134 eterization which aims at representing the impact of the unresolved mesoscale processes
135 in a coarse-resolution ocean model. Finally, we conclude in section 4 on the practical use
136 of this three-dimensional parameter space and discuss its strengths and limitations.

2 Materials and Methods

2.1 Definition of the Three Dimensionless Numbers

We will formulate three dimensionless numbers to characterize the evolution of the mixed layer depth h of a 1D water column model that evolves from one day to another according to daily-mean surface forcings and preconditioning conditions. The goal here is to identify the main factors that drive the MLD evolution $\partial_t h$ in order to build a parameter space with a small number of dimensions being usable for evaluating $\partial_t h$. The principal omissions resulting from our choices will be discussed further in section 2.2.

We adopt the description of the water column given by bulk mixed layer models (e.g. Pollard et al., 1973): near the surface, we consider a well-mixed layer of thickness h . This layer is forced at the surface by the wind stress with a friction velocity $u_* = [(\overline{u'w'}|_{z=0})^2 + (\overline{v'w'}|_{z=0})^2]^{1/4}$ and the downward surface buoyancy flux $B_0 = -\overline{w'b'}|_{z=0}$ ($B_0 < 0$ for a destabilizing flux at the ocean surface), with u' , v' and w' the turbulent velocities, the overline that denotes an average over small scale fluctuations (see Stull, 1988), b' the fluctuation of the buoyancy $b = -\frac{\rho - \rho_0}{\rho_0}g$, ρ the density, ρ_0 the reference density, and g the acceleration due to gravity. At the base of the mixed layer, the stratification is given by the Brunt Vaisala frequency N_h , which is sometimes called "preconditioning". In order to describe the MLD evolution, we have also opted to retain the local Coriolis parameter f . With this idealized view of the mixed layer, the MLD evolution $\partial_t h$ is a function of five physical quantities: (u_*, B_0, h, N_h, f) . These 5 physical quantities are expressed with 2 distinct dimensions: length and time ($[u_*] = L.T^{-1}$, $[B_0] = L^2.T^{-3}$, $[h] = L$, $[N_h] = T^{-1}$, $[f] = T^{-1}$). The Vaschy-Buckingham theorem (π theorem) thus states that these five physical quantities can be represented by $5 - 2 = 3$ dimensionless numbers. The three dimensionless numbers we have chosen are

$$\lambda_s = \frac{-B_0 h}{u_*^3}, \quad (1)$$

$$R_h = \left(\frac{N_h h}{u_*} \right)^2, \quad (2)$$

and

$$f/N_h. \quad (3)$$

162 Note that λ_s is positive for a destabilizing surface buoyancy flux ($B_0 < 0$) and nega-
 163 tive for a stabilizing surface buoyancy flux ($B_0 > 0$).

164 Henceforth, we describe the physical interpretations of these three dimensionless
 165 numbers and then present the associated three-dimensional parameter space.

166 **2.1.1 Physical Interpretation of λ_s**

167 In the context of ocean mixed layer dynamics, λ_s can be interpreted in at least three
 168 ways.

169 *1st Interpretation:* λ_s can be interpreted using the evolution equation of the Tur-
 170 bulent Kinetic Energy (TKE; for a full description of this equation, see Hanjalić & Laun-
 171 der, 1972; Rodi, 1987; Umlauf & Burchard, 2003):

$$\frac{Dk}{Dt} = P + G - \epsilon + \mathcal{D}_k \quad (4)$$

172 with $k = \frac{1}{2}(\overline{u'^2} + \overline{v'^2} + \overline{w'^2})$ the TKE, $P = -\overline{u'w'}\partial_z\bar{u} - \overline{v'w'}\partial_z\bar{v}$ the TKE produc-
 173 tion by the shear (by conversion of mean kinetic energy), $G = \overline{w'b'}$ the TKE produc-
 174 tion (or destruction) by the turbulent buoyancy flux (by conversion of mean potential
 175 energy), ϵ the TKE dissipation, and \mathcal{D}_k the TKE diffusion.

176 The surface layer is defined as the zone where the turbulent fluxes vary by less than
 177 10% from their values at $z = 0$ (Stull, 1988). In this zone, we can consider $\overline{u'w'} \approx \overline{u'w'}|_{z=0} \propto$
 178 u_*^2 and $G \approx \overline{w'b'}|_{z=0} = -B_0$. Since the surface mean horizontal velocity $\bar{u}|_{z=0}$ is well
 179 correlated to the surface friction velocity u_* (Weber, 1983), and if we neglect the mean
 180 horizontal velocity \bar{u} below the mixed layer depth (Pollard et al., 1973), then an order
 181 of magnitude of $\partial_z\bar{u}$ is given by u_*/h . It follows $P \propto u_*^3/h$. An evaluation of G/P in
 182 the surface layer finally gives

$$\left. \frac{G}{P} \right|_{surf} \propto \frac{-B_0}{\left(\frac{u_*^3}{h}\right)} \equiv \lambda_s. \quad (5)$$

183 This ratio $G/P|_{surf}$ is by definition the flux Richardson number R_f evaluated in
 184 the surface layer (Mellor & Durbin, 1975). It gives the relative contribution of surface
 185 buoyancy flux and wind for the production of TKE. In the case $B_0 < 0$ *i.e.* $G/P|_{surf} >$
 186 0 , both terms produce TKE. On the other hand, in the case of a restratifying buoyancy

187 flux $B_0 > 0$, there is a competition between production by the shear ($P > 0$) and de-
 188 struction by the turbulent buoyancy flux ($G < 0$). Particularly, for $G/P|_{surf} < -1$,
 189 more TKE is destroyed (converted into mean potential energy) than created (from mean
 190 kinetic energy): this likely represents a restratification event.

191 *2nd Interpretation:* We can also interpret λ_s in the light of the Monin-Obukhov
 192 similarity theory (Obukhov, 1971). This theory, which is valid in the surface layer, in-
 193 troduces the Monin-Obukhov length L_{MO} :

$$L_{MO} = \frac{u_*^3}{\kappa B_0}. \quad (6)$$

194 We give here its definition in the oceanic framework (see for example Zheng et al.,
 195 2021) which is the opposite of the atmospheric definition. The physical interpretation
 196 of L_{MO} was introduced by Obukhov in the case $L_{MO} < 0$ ($\Leftrightarrow B_0 < 0 \Leftrightarrow \lambda_s > 0$). In
 197 this regime, L_{MO} estimates the typical thickness of a "sub-layer of dynamic turbulence"
 198 in which stratification is of little importance and the turbulence dynamics is governed
 199 by the mean-current shear (Obukhov, 1971), *i.e.* the production of TKE by the buoy-
 200 ancy G is negligible in comparison to the one by the mean-current shear P . In practice,
 201 Wyngaard (1973) has shown that $G \simeq P$ for $z \simeq 0.5L_{MO}$ (Fig 5.22 Stull, 1988). The
 202 number λ_s can be seen as

$$\lambda_s = \frac{1}{\kappa} \frac{-h}{L_{MO}}. \quad (7)$$

203 Thus, $\lambda_s < 0.5/\kappa$ gives $P > G$ in the mixed layer while $\lambda_s > 0.5/\kappa$ means $G >$
 204 P . It is important to recall that this interpretation only stands for $L_{MO} < 0$ ($\Leftrightarrow B_0 <$
 205 $0 \Leftrightarrow \lambda_s > 0$). For the case $L_{MO} > 0$ ($\Leftrightarrow B_0 > 0 \Leftrightarrow \lambda_s < 0$), we refer to our first inter-
 206 pretation of λ_s .

207 *3rd Interpretation:* In the case $B_0 < 0$, convective thermals have a velocity in
 208 the order of $w_* = (-B_0 h)^{1/3}$ (Willis & Deardorff, 1974; Marshall & Schott, 1999). Then
 209 λ_s can be written as

$$\lambda_s = \left(\frac{w_*}{u_*} \right)^3. \quad (8)$$

210 In this expression, it is clear that λ_s measures the relative importance of mechan-
 211 ical and convective forcings.

212 Last, it is worth noting that in a different context Simpson and Hunter (1974) used
 213 a similar ratio to characterize the mixing occurring in the Irish Sea where u_* was related
 214 to the tidal forcing (friction in the bottom boundary layer).

215 **2.1.2 Physical Interpretation of R_h**

216 The dimensionless number R_h can be interpreted as a Richardson number. By def-
 217 inition the gradient Richardson number $Ri = N^2/(\partial_z \bar{u})^2$ is the ratio of the stabilizing
 218 effect of the stratification and the destabilizing effect of the shear of the mean current
 219 (see for example Mack & Schoeberlein, 2004). We compare here the stratification at the
 220 mixed layer base N_h^2 with the order of magnitude of the wind-induced shear u_*/h . This
 221 gives the ratio:

$$\frac{N_h^2}{\left(\frac{u_*}{h}\right)^2} \equiv R_h. \quad (9)$$

222 We could have included the contribution of w_* to the shear but we will see in sec-
 223 tion 2.3 that this omission is intentional and results in a simpler interpretation of the
 224 parameter space.

225 **2.1.3 Physical Interpretation of f/N_h**

226 In the context of mixed layer dynamics, there are several interpretations for the
 227 dimensionless number f/N_h .

228 First, the ratio f/N_h can be seen as h/L_d , where $L_d \propto Nh/f$ is the "mixed layer"
 229 Rossby radius of deformation in the quasi-geostrophic context (h is not the total depth
 230 of the fluid but the mixed layer depth). In the situation where $f/N_h > O(1)$, we ex-
 231 pect that mixed layer instabilities will create a lateral buoyancy flux (see Boccaletti et
 232 al., 2007). Part of the turbulent energy normally used for vertical mixing is hence used
 233 for lateral mixing. Therefore, we expect that values $f/N_h > O(1)$ result in a slowdown
 234 of the MLD deepening. In the specific context of the free convection regime, rapid ro-
 235 tation is also known to decrease the turbulent heat flux (see Bouillaut et al., 2019; Au-
 236 rnou et al., 2020), and so we expect that for high values of f/N_h , we are likely to ob-

237 serve a reduced MLD deepening. Finally, one last possible interpretation of f/N_h was
 238 given by Speer and Marshall (1995) who have described how the aspect ratio of convec-
 239 tive plumes is determined by the ratio f/N_h , where the effect of rotation is mainly to
 240 alter the lateral spreading of convective structures (see also Deremble, 2016).

241 **2.2 Limitations**

242 There are of course other physical phenomena that occur in the mixed layer and
 243 that we have not taken into account:

- 244 • The effect of waves and associated Langmuir turbulence that could have been rep-
 245 resented through the values of the surface Stokes drift u_0^S (Q. Li et al., 2019). How-
 246 ever, it is worth mentioning that part of u_0^S can be explained by u_* . Minimal pa-
 247 rameterizations of Langmuir turbulence even define u_0^S directly proportional to
 248 u_* (M. Li & Garrett, 1993; Madec et al., 2022). Thus, some of the wave impacts
 249 are implicitly contained through the consideration of u_* .
- 250 • All the effects of the horizontal gradients (of velocities, pressure...) and advections
 251 that are present in a 3D realistic ocean model. We can particularly pinpoint the
 252 Ekman flow that can create an equivalent stabilizing/destabilizing wind-driven buoy-
 253 ancy flux (see for example Thomas & Lee, 2005), and the impacts of the restrat-
 254 ification by baroclinic instability at convective fronts or at mesoscale eddy fronts.
 255 Some of these aspects can be captured by looking at the isopycnal slopes and this
 256 point will be further discussed in section 3.3.
- 257 • The influence of the vertical shear of the horizontal velocities. As we work with
 258 daily evolution, and knowing the Ekman theory (Ekman, 1905), we can expect this
 259 shear to be partly represented by the consideration of the surface wind friction ve-
 260 locity, the mixed layer depth, and the Coriolis parameter.

261 Considering many of these aspects would have meant adding more dimensions to
 262 the parameter space and thus reducing its practical use. We will see in the results that
 263 the dimensionless numbers we have chosen are in many situations sufficient to obtain a
 264 significant prediction of the MLD evolution and therefore capture well the dominant pro-
 265 cesses of this evolution.

266

2.3 Other Possible Dimensionless Numbers

267

268

We have defined three dimensionless numbers from the five physical quantities (u_*, B_0, h, N_h, f) , but other choices could have been possible. We want to highlight here some of them:

269

270

271

272

273

274

275

276

277

278

279

- The Rossby number $Ro = u_*/(hf)$ that characterizes the relative importance of the inertial and the Coriolis forces (Van Der Laan et al., 2020).
- The ratio h/h_{\max} with $h_{\max} = 2^{0.75}u_*/\sqrt{Nf}$ which compares the current h to the maximum one h_{\max} predicted by Pollard et al. (1973) in case of a shear-driven MLD deepening in a rotating case. It is known that h does not really stop at h_{\max} but this value represents an important threshold of the deepening (Ushijima & Yoshikawa, 2020).
- In case of $B_0 < 0$, the Richardson number $R_h^* = (N_h h/w_*)^2$ constructed with w_* rather than u_* which compares the stabilizing effect of the stratification and the destabilizing impact of the buoyancy flux (Turner, 1986; Shy, 1995). However, R_h^* can be expressed as

$$R_h^* = R_h/\lambda_s^{2/3} \quad (10)$$

280

281

282

283

284

285

286

and hence, in a log-log parameter space (λ_s, R_h) , we will see that the isolines of R_h^* appear as lines of slope 2/3. Then, we have the possibility to see the isolines of both R_h and R_h^* at the same time in the parameter space. We will use this information to decide whether one or the other is more representative of the deepening situation. This would have been impossible if we had taken a Richardson number defined with the two contributions at the same time, such as $(N_h h/\sqrt{u_* w_*})^2$, $(N_h h/\max(u_*, w_*))^2$ or $(N_h h/(u_* + w_*))^2$.

287

288

289

290

291

292

The next four sections present the simulations we will use to evaluate the parameter space and to conduct the two model sensitivity studies. In the next three sections, we present three 3D realistic ocean simulations at three different horizontal resolutions (1/60°, 1/12°, and 1°). These simulations will be used to study the impact of the horizontal resolutions on the MLD evolution regimes. Table 1 summarizes the main features of these simulations.

2.4 NEMO-eNATL60 1/60° Basin-scale North Atlantic Ocean Simulation

The eNATL60-BLBT02 (eNATL60) simulation (Brodeau et al., 2020) is a basin-scale North Atlantic ocean/sea-ice simulation forced by the atmospheric 3-hourly ERA-Interim reanalysis (Dee et al., 2011) on a 1/60°-horizontal and 300-vertical-level grid. It includes an explicit tidal forcing. The lateral boundary conditions for the ocean velocities, temperature, and salinity are based on the GLORYS12 v1 reanalysis (Lellouche et al., 2021). Vertical mixing is governed by a Turbulent Kinetic Energy (TKE) scheme combined with the Enhanced Vertical Diffusivity (EVD) parameterization which increases the vertical diffusivity in case of unstable water columns (Lazar et al., 1999; Madec et al., 2022). The Fox-Kemper parameterization (Fox-Kemper et al., 2007), which represents the restratifying effect of sub-mesoscale mixed layer eddies, is included. The model outputs, ignoring the spin-up period, cover 10 months from 1 January 2010 to 29 October 2010. A description of the technical choices and the configuration files are available at <https://github.com/ocean-next/eNATL60>. For our study, we extracted daily averages of the data in two regions of interest (Figure 1). The "Western Mediterranean region" extends from 2°E to 10°E and from 40°N to 44°N, and the "Labrador region" from 56°W to 51°W and from 55°N to 59°N. To avoid shallow water coastal dynamics, we only kept locations for which the local depth is greater than or equal to 2000 m. Moreover, to reduce the amount of data, we subsampled the horizontal resolution of the outputs from 1/60° to 1/12°. For doing that, we used the function "samplegrid" of the Climate Data Operators library (CDO; Schulzweida, 2023) with a subsampling factor of 5 on both x and y dimensions of the grid.

2.5 NEMO ORCA 1/12° Global Ocean Simulation

The eORCA12.L75-GJM2020 (eORCA12) simulation is a global ocean/sea-ice simulation forced by the atmospheric reanalysis JRA55-do 1.4.0 (Tsujino et al., 2018) performed on the ORCA12.L75 grid (1/12° horizontal resolution and 75-level non-uniform vertical grid) over the period 1979-2019. Vertical mixing is governed by a TKE + EVD + IWM (additional parameterization accounting for mixing due to internal waves) scheme. A description of the technical choices and the configuration files are available at <https://github.com/meom-configurations/eORCA12.L75-GJM2020>. In this study, we used a 10-year period (1 January 2006 to 1 January 2015) and we extracted daily averages of

Table 1. Summary of the main features of the simulations. "Med" and "Lab" stand for respectively the "Western Mediterranean" and the "Labrador" extractions (see text)

Simulation	Horizontal resolution [[Subsampling]]		Total time		Vertical mixing scheme	Additional parameterization	Reference
	Med/Lab	Global	Med/Lab	Global			
eNATL60	1/60° [[1/12°]]	-	10 months (Jan to Oct 2010)		TKE + EVD	Fox-Kemper	Brodeau et al., 2010 (https://github.com/ocean-next/eNATL60)
eORCA12	1/12°	[[15°]]	10 years (2006 to 2015)		TKE + EVD	Internal Wave Mixing (IWM)	https://github.com/meom-configurations/eORCA12.L75-GJM2020
eORCA1	1°	[[15°]]	20 years (2000 to 2019)		TKE + EVD	-	https://github.com/meom-configurations/eORCA1-GJM2020
eORCA1GM	1°	[[15°]]	20 years (2000 to 2019)		TKE + EVD	Gent McWilliams (GM)	https://github.com/meom-configurations/eORCA1-GJM2020
Collection of 1D simulations	-	-	20 years (2006 to 2015)	10 years (2000 to 2019)	TKE + EVD	-	https://github.com/legaya/James2023_ParameterSpace/

324 the data on the same Western Mediterranean and Labrador regions as described above
325 (Figure 1), with the same restriction of keeping only locations for which the local depth
326 is greater than or equal to 2000 m. Unlike eNATL60, which is not a global simulation,
327 we are also going to use the results of eORCA12 at the global scale and, to reduce the
328 amount of data, we subsampled the outputs from the 1/12° resolution to only keep 234
329 points placed on a 15° grid (cf Figure 1). This coarse representation is enough to cap-
330 ture a realistic range of f/N_h , representative of the world's oceans.

331 2.6 NEMO ORCA 1° Global Ocean Simulation

332 We performed the eORCA1-GJM2020 (eORCA1) simulation in a set-up that is the
333 same as the eORCA12 simulation, except for the horizontal resolution. However, a 1°
334 horizontal resolution is not considered eddy-resolving and for this reason, an eddy-induced
335 velocity is often added at this resolution to parameterize missing mesoscale eddies. We
336 computed this eddy-induced velocity with the Gent McWilliams (GM) parameterization
337 (Gent & McWilliams, 1990). We performed two experiments, eORCA1 without GM and
338 eORCA1GM with GM. The GM coefficient was taken constant (with the NEMO default
339 input parameters of lateral diffusive velocity $Le = 0.02 \text{ m s}^{-1}$ and lateral diffusive veloc-
340 ity $Ue = 2 \times 10^5 \text{ m}$). A description of the technical choices and the configuration files
341 are available at <https://github.com/meom-configurations/eORCA1-GJM2020>. We took
342 daily averages of the outputs over 20 years from 1 January 2000 to 1 January 2019. We
343 extracted the outputs on the two regions of interest, as well as at the global scale sub-

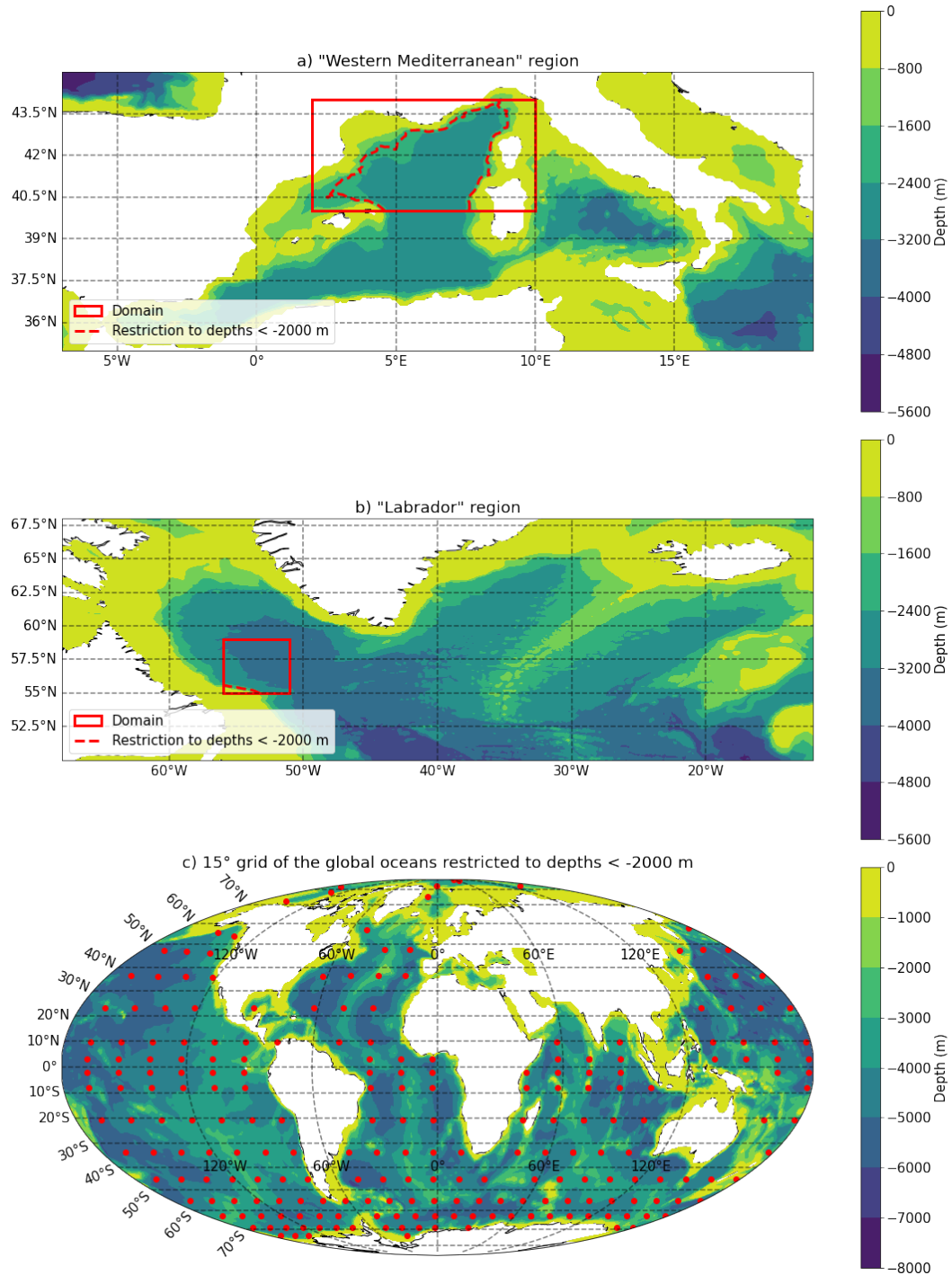


Figure 1. The three regions of interest in this study. a) and b) are respectively the "Western Mediterranean" region that extends from 2°E to 10°E and from 40°N to 44°N, and the "Labrador" region that extends from 56°W to 51°W and from 55°N to 59°N. c) presents the 15° grid used at the global scale (Mollweide's projection). All of these three regions are restricted to depths greater than 2000 m.

344 sampled on the 15° grid described in the previous section. Again, only the locations for
 345 which the local depth is greater than or equal to 2000 m were kept.

346 2.7 1D Simulations

347 This section presents the 1D simulations we will use to classify the MLD evolution
 348 regimes in the parameter space.

349 We performed a collection of 1D water column simulations using the code presented
 350 in Fearon et al. (2020), which is a standalone 1D vertical version of the Coastal and Re-
 351 gional Ocean COmmunity model (CROCO, <https://www.croco-ocean.org/>). This col-
 352 lection contains 20-year simulations from 1 January 2000 to 1 January 2019 at all the
 353 1° grid locations of the two regions Labrador and Western Mediterranean, as well as 10-
 354 year simulation from 1 January 2006 to 1 January 2015 for all the points of the global
 355 subsampled grid of 15° resolution. To be consistent with the 3D models, we used a TKE
 356 + EVD scheme, we included the Earth’s rotation, we kept only the locations where the
 357 local depth is greater than 2000 m and we applied the same atmospheric forcings as
 358 the eORCA1 simulation (presented in section 2.6). The wind, precipitation, evaporation,
 359 and non-solar heat flux forcings were applied daily with 24-hour constant values. The
 360 solar flux was constructed with a cosine truncated of its negative values, thus represent-
 361 ing 12 h daytime with positive values and 12 h nighttime with zero values. The temper-
 362 ature and salinity profiles were re-initialized to their eORCA1 values at the beginning
 363 of each new year, so these simulations should be viewed as multiple annual simulations.
 364 The vertical grid was taken equal to the one of eORCA1/eORCA12 cut at 2000 m depth,
 365 hence the 54 shallowest levels of this 75-level grid. The time step was set to 360 s. The
 366 UNESCO 1983 nonlinear equation of state was used (Fofonoff & Millard Jr, 1983). At
 367 the bottom boundary of the domain, we imposed a homogeneous Neumann condition
 368 (no flux).

369 2.8 Practical Calculation of the Dimensionless Numbers

370 The five physical quantities (u_*, B_0, h, N_h, f) appearing in the dimensionless num-
 371 bers are calculated as follows:

- 372 • The surface wind friction velocity is calculated from its definition $u_* = \sqrt{|\tau^w|/\rho_0}$
 373 with $|\tau^w|$ the norm of the wind stress vector at the ocean surface.

- 374 • We calculate the surface buoyancy flux with its classical linear definition: $B_0 =$
 375 $\frac{g}{\rho_0} \left(\frac{\alpha Q}{c_p} - \beta S_{surf}(E - P) \right)$ with Q the downward surface heat flux ($Q < 0$ for
 376 cooling), E the evaporation, P the precipitation, c_p the heat capacity per unit mass,
 377 S_{surf} the surface salinity, ρ_0 the reference density, and (α, β) respectively the ther-
 378 mal expansion coefficient and the haline contraction coefficient of the linearized
 379 equation of state $\rho = \rho_0(1 - \alpha(T - T_0) + \beta(S - S_0))$ with T_0 the reference temper-
 380 ature and S_0 the reference salinity. These two coefficients (α, β) are calculated
 381 for each location at every time step according to the local values of the surface tem-
 382 perature and the surface salinity.
- 383 • We choose the classical MLD definition of the CMIP6 working group for h (Griffies
 384 et al., 2016, Appendix H2.4.2). This definition is based on a buoyancy difference
 385 from the surface and was designed to give results similar to the density criterion
 386 of a 0.03 kg/m^3 difference of de Boyer Montégut et al. (2004) in the case of a lo-
 387 cal density close to 1035 kg/m^3 .
- 388 • The stratification at the base of the mixed layer N_h^2 is defined as a difference be-
 389 tween the properties at the MLD ($z = -h$) and 10 % below the MLD ($z = -1.1h$):

$$N_h^2 = \frac{g}{\rho_0} \frac{\rho(z = -1.1h) - \rho(z = -h)}{0.1h}. \quad (11)$$

390 It is worth mentioning here that, if we interpret $\Delta\rho = \rho(z = -1.1h) - \rho(z =$
 391 $-h)$ as the "density jump" at the base of the mixed layer, $R_h = (N_h h / u_*)^2$ can
 392 be written as $R_h = g \frac{\Delta\rho}{\rho_0} h / (0.1 u_*^2)$ and is hence proportional to $R_\tau = g \frac{\Delta\rho}{\rho_0} h / u_*^2$
 393 the bulk Richardson number associated to the wind (Price, 1979).

- 394 • The Coriolis parameter is equal to $f = 2\Omega_0 \sin(\phi)$ with $\Omega_0 = 7.29 \times 10^{-5} \text{ rad s}^{-1}$
 395 the rotation rate of the Earth and ϕ the latitude. As we did not consider any lat-
 396 eral gradients, the sign of f is of course not important in our context and we thus
 397 consider the absolute value of f . However, throughout the manuscript, we write
 398 f rather than $|f|$ for brevity.

399 Sensibility of the results to other choices of MLD definitions (de Boyer Montégut
 400 et al., 2004; Reichl & Hallberg, 2018) and other N_h^2 evaluations (centered at $z = -h$
 401 or with a constant distance of 15 m below the MLD, see the discussion in Sérazin et al.,
 402 2023) were tested but not shown here for brevity. In short, the two definitions we chose
 403 were the ones giving the results with the highest significance (the notion of "significance"

404 in the parameter space is defined in the next section) and hence the ones that are the
 405 more relevant in our context of the evaluation of the relative MLD deepening or shoal-
 406 ing over a 1-day period.

407 As we follow the MLD evolution over a 1-day period, we use the daily averages of
 408 the quantities (from noon to noon). We opt to take the daily averages of h and N_h^2 at
 409 day $d-1$, and u_* and B_0 at day d . The reason is that h and N_h^2 represent an initial state,
 410 with a MLD h in which thermals can develop underlying a stable stratification N_h^2 . This
 411 initial state is modified by a whole day of forcing of u_* and B_0 . Hence, the temporal evo-
 412 lutions of the MLD $\partial_t h$ are computed over this 1-day period (day $d-1$ to day d). Fi-
 413 nally, we note that the calculation of $\Delta\rho = \rho(z = -1.1h) - \rho(z = -h)$, needed to ob-
 414 tain N_h^2 (see Equation 11), can present two problems. First, N_h^2 can be negative if there
 415 is an instability at the base of the mixed layer. These cases represent less than 0.01 %
 416 of the points and are simply discarded. Second, the calculation of $\Delta\rho$ is not defined if
 417 the mixed layer reaches the bottom of the domain. These points, which correspond to
 418 a zero $\partial_t h$ evolution, also represent less than 0.01 % of all cases and are discarded as well.

419 2.9 Visualization in the Parameter Space

420 We characterize the MLD evolution through the relative change of the MLD $\partial_t h/h$,
 421 expressed in %/day. This variable is not dimensionless and could have been normalized
 422 by dividing by a characteristic time t_c . Several possibilities were tested. However, since
 423 this change makes it more difficult to understand the variable, and since none of the tri-
 424 als produced any improvement in the results, none of the possibilities were retained.

425 The parameter space has three dimensions: λ_s , R_h , and f/N . For exploring these
 426 three dimensions, we use projections into two-dimensional parameter spaces $\lambda_s - f/N$,
 427 $R_h - f/N$, and $\lambda_s - R_h$. To facilitate the intercomparison of two graphs, we use hexag-
 428 onal bin plots rather than scatter plots and we define four MLD evolution classes accord-
 429 ing to the value of $\partial_t h/h$. Comparing two graphs can then be done by looking at the MLD
 430 evolution class obtained hexagon by hexagon. The four MLD evolution regimes are de-
 431 fined as follows

- 432 • $\partial_t h/h \geq 10$ %/day: **Strong Deepening**
- 433 • 1 %/day $\leq \partial_t h/h < 10$ %/day: **Deepening**

- 434 • $-1\%/day \leq \partial_t h/h < 1\%/day$: **Stable**
- 435 • $\partial_t h/h < -1\%/day$: **Restratification**

436 The class of a hexagon is determined by the majority class of its constituent points.
 437 That is, for every hexagon of a 2D parameter space we sort all the points inside this hexagon
 438 in one of the 4 classes and the class of the hexagon is the one that is the most represented.
 439 If this class represents more than 75% of the points, it is tagged as "highly significant".
 440 If this percentage is between 50% and 75%, it is tagged as "significant". If it is below
 441 50%, it is considered not significant. For statistical reasons, a hexagon is kept only if it
 442 contains at least 30 points.

443 3 Results

444 In this section, we populate the 3D parameter space $(\lambda_s, R_h, f/N_h)$ with 1D sim-
 445 ulations performed at the global scale and we show that considering only the two dimen-
 446 sions (λ_s, R_h) is the best choice of 2D projection of this 3D parameter space. We then
 447 focus on this two-dimensional $\lambda_s - R_h$ parameter space and we present how this frame-
 448 work can be used to analyze 3D realistic ocean simulations. The first application is about
 449 the impact of the lateral resolution on the MLD evolution regimes. The second appli-
 450 cation focuses on the effect of the Gent McWilliams parameterization which aims at rep-
 451 resenting the impact of the unresolved mesoscale processes in a coarse-resolution ocean
 452 model.

453 3.1 Evaluation of the Three-Dimensional Parameter Space

454 The three-dimensional parameter space $\lambda_s - R_h - f/N_h$ is evaluated with 1D sim-
 455 ulations performed at the locations of the 15° global grid (described in section 2.7). We
 456 first show that the (λ_s, R_h) projection is the best choice of 2D projection of this 3D pa-
 457 rameter space. We then highlight the influence f/N_h .

458 Figure 2 displays the three two-dimensional projections of the 3D parameter space
 459 $\lambda_s - R_h - f/N_h$. Among these three projections, the 2D parameter space $\lambda_s - R_h$ exhibits
 460 the highest significance with the MLD evolution classes of its hexagons being significant
 461 in 96% of the cases. In comparison, the significance is 84% for the $f/N_h - R_h$ projec-
 462 tion and 73% for the $\lambda_s - f/N_h$ projection (definition of the "significance" in section 2.9).

Table 2. Significances of the MLD evolution classes of the hexagons for the three 2D projections of the 3D parameter space $\lambda_s - R_h - f/N_h$

2D parameter space	$\lambda_s - R_h$	$f/N_h - R_h$	$\lambda_s - f/N_h$
Highly significant hexagons	74 %	46 %	30 %
Significant hexagons	22 %	38 %	43 %
Not significant hexagons	4 %	16 %	27 %

463 Moreover, among these significant hexagons, the $\lambda_s - R_h$ parameter space shows the high-
 464 est number of highly significant hexagons: 74 % of all hexagons (46 % for $f/N_h - R_h$; 30 %
 465 for $\lambda_s - f/N_h$; cf Table 2).

466 In addition to the high significance levels, the $\lambda_s - R_h$ projection also exhibits the
 467 best "spatial coherence": the four MLD evolution regimes are organized in well-delimited
 468 continuous zones. The main thresholds delineating these zones are plotted in Figure 2.a.
 469 and are as follows:

- 470 • **Vertical threshold at $\lambda_s = -3$:** Physically, we expect restratification for $G/P|_{surf} <$
 471 -1 , indicating that the surface buoyancy flux removes more TKE than the amount
 472 produced by the wind. In terms of λ_s (that is $\propto G/P|_{surf}$), the threshold seems
 473 to be around $\lambda_s \approx -3$. The criterion $\lambda_s < -3$ corresponds to stable or restrat-
 474 ification regimes and is consistent with a TKE-loss situation. This $\lambda_s < -3$ thresh-
 475 old is also observed in the $\lambda_s - f/N_h$ parameter space and so does not depend on
 476 f/N_h .
- 477 • **Horizontal thresholds in the range $-3 < \lambda_s < 0$:** In the range $-3 < \lambda_s <$
 478 0 , the boundaries are horizontal, indicating that, when the wind dominates over
 479 the buoyancy flux, only the value of R_h is important for predicting the MLD evo-
 480 lution regime. A value of $R_h > 1000$ corresponds to "stable" regime, $1000 < R_h <$
 481 300 corresponds to "deepening" regime and $R_h < 300$ corresponds to "strong deep-
 482 ening" regime. This progression according to R_h corresponds to the traditional
 483 interpretation of a Richardson number. For High values of R_h , the shear u_* / h is
 484 too weak to erode the pycnocline stratification N_h , leading to a stable regime. In
 485 contrast, low values of R_h result in MLD deepening regimes.

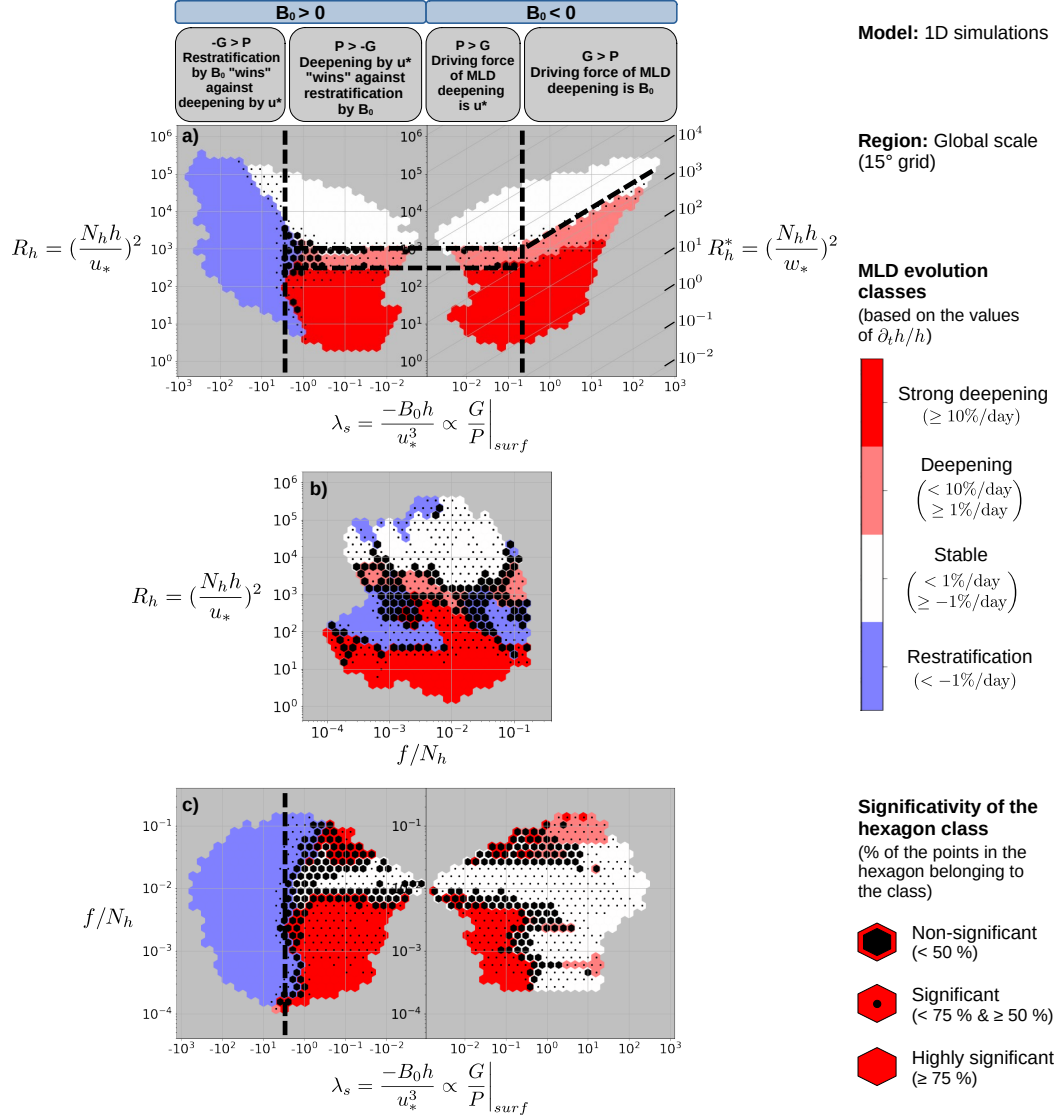


Figure 2. Results of the 1D simulations performed at the locations of the 15° global grid, plotted in the three different 2D projections of the 3D parameter space: (a) $\lambda_s - R_h$, (b) $f/N_h - R_h$ and (c) $\lambda_s - f/N_h$. The MLD evolution classes are defined based on the values of $\partial_t h/h$. The "strong deepening" class is defined by $\partial_t h/h \geq 10\%/day$, "deepening" by $1\%/day \leq \partial_t h/h < 10\%/day$, "stable" by $-1\%/day \leq \partial_t h/h < 1\%/day$ and "restratification" by $\partial_t h/h < -1\%/day$. The class of a hexagon is the majority class of its constituent points. If this majority class represents less than 50% of the constituent points, the hexagon is tagged "non-significant" (superimposed black hexagon), if it is between 50% and 75% it is "significant" (superimposed black dot) and if it is higher than 75% it is "highly significant" (nothing superimposed). A grid representing the slope 2/3 isolines of R_h^* is added in the $\lambda_s > 0$ panel of the $\lambda_s - R_h$ parameter space. Dashed lines highlight demarcations between MLD evolution regimes discussed in the text.

486 • **Horizontal thresholds and sloping lines in the zone $\lambda_s > 0$:** The demar-
487 cations remain horizontal for $\lambda_s < 0.2$. Beyond that, for $\lambda_s > 0.2$, demarcations
488 follow lines with a 2/3 slope, which are isolines of $R_h^* = (N_h h/w_*)^2$. In this zone
489 where $\lambda_s > 0.2$, only the value of the buoyancy-flux related Richardson number
490 R_h^* is important for predicting the MLD evolution regime. A value $R_h^* > 3000$
491 indicates a stable regime, while low values suggest deepening or strong deepening
492 regimes. The fact that R_h^* is the important dimensionless number in the $\lambda_s >$
493 0.2 zone informs us that this zone is a buoyancy-flux-dominant zone ($G > P$).
494 To summarize the previous points, λ_s indicates a restratifying TKE-loss zone for
495 $\lambda_s < -3$ and a TKE-gain zone for $\lambda_s > -3$. The TKE-loss zone is buoyancy-
496 flux-dominant whereas the TKE-gain zone is either wind-dominant for $-3 < \lambda_s <$
497 0.2 and represented by demarcations by R_h , or buoyancy-flux-dominant for $\lambda_s >$
498 0.2 and represented by demarcations defined with R_h^* . For clarity, these interpre-
499 tations based on G and P are added on the top of Figure 2.a.

500 While the $\lambda_s - R_h$ projection is the best 2D projection of the 3D parameter space,
501 we also explore the third dimension within this space. We sort the results according to
502 their f/N_h values and we plot different "slices" of the parameter space in Figure 3.

503 The influence of rotation, as assessed by the parameter f/N_h , appears to stabilize
504 the water column. To illustrate this effect, we highlight in Figure 3 the demarcations be-
505 tween the stable regime and the deepening regime. We also plot in Figure 4 the value
506 of these thresholds $R_{h,c}$ and $R_{h,c}^*$ as a function of f/N_h (normalized by their values $R_{h,c0}$
507 and $R_{h,c0}^*$ for $f/N_h \in [10^{-3.5}; 10^{-3.0}]$). The higher f/N_h , the lower are $R_{h,c}$ and $R_{h,c}^*$.
508 Consequently, in the presence of rotation, a weaker stratification and/or a higher forc-
509 ing (u^*/h or w^*/h) are required to achieve the same level of deepening as without ro-
510 tation. This reduced effective surface buoyancy/wind power input could be attributed
511 to the generation of inertial oscillations (Pollard et al., 1973) or by enhanced lateral buoy-
512 ancy flux (Boccaletti et al., 2007).

513 Rotation has a more pronounced effect on the wind forcing than the buoyancy forc-
514 ing because $R_{h,c}$ decreases more with f/N_h than $R_{h,c}^*$ (cf Figure 4). Hence, the region
515 for which the MLD deepening is driven by the wind narrows with f/N_h compared to the
516 region for which the MLD deepening is driven by the surface buoyancy forcing. The $\lambda_{s,c}$
517 thresholds that delineate these two regions are plotted in Figure 3 and their correspond-

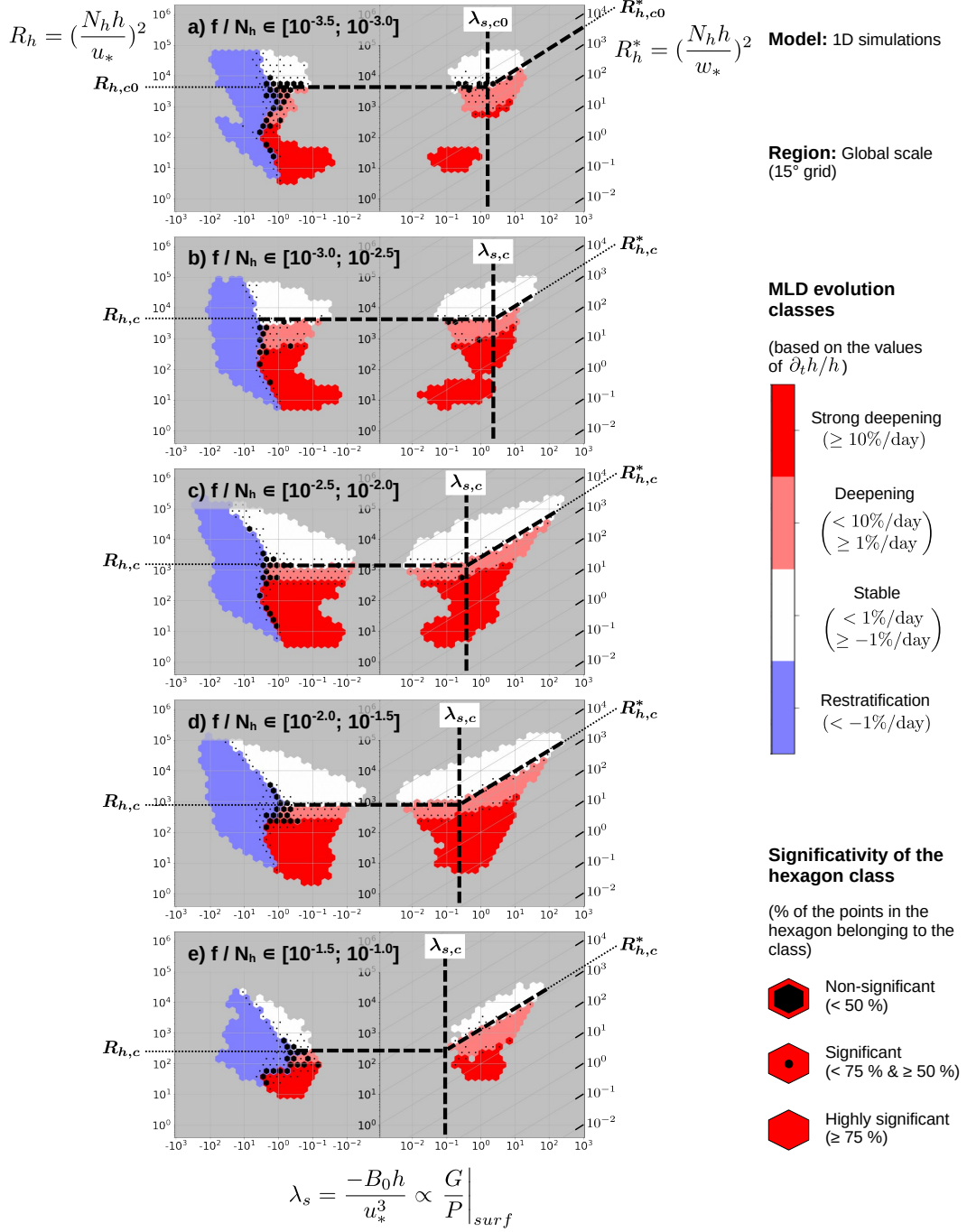


Figure 3. Results of the 1D simulations performed at the locations of the 15° global grid plotted in the $\lambda_s - R_h$ parameter space. The results are filtered according to their f/N_h values: (a) $f/N_h \in [10^{-3.5}; 10^{-3.0}]$, (b) $f/N_h \in [10^{-3.0}; 10^{-2.5}]$, (c) $f/N_h \in [10^{-2.5}; 10^{-2.0}]$, (d) $f/N_h \in [10^{-2.0}; 10^{-1.5}]$ and (e) $f/N_h \in [10^{-1.5}; 10^{-1.0}]$. Dashed lines highlight the thresholds $R_{h,c}$ and $R_{h,c}^*$ between the stable and the deepening regimes, and $\lambda_{s,c}$ the limit between the wind-dominant and the surface-buoyancy-flux-dominant zones. Values $R_{h,c0}$, $R_{h,c0}^*$ and $\lambda_{s,c0}$ are the ones for $f/N_h \in [10^{-3.5}; 10^{-3.0}]$. Other graphical conventions as in Figure 2.

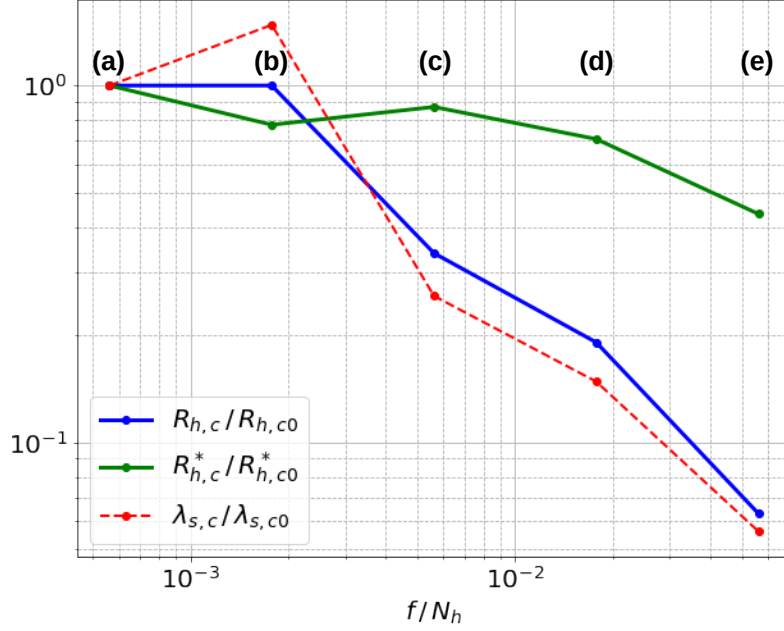


Figure 4. Dependence on f/N_h of the three demarcation thresholds $R_{h,c}$, $R_{h,c}^*$ and $\lambda_{s,c}$. The thresholds $R_{h,c}$ and $R_{h,c}^*$ indicate the demarcation between the stable and the deepening regimes respectively in the wind-dominant zone and in the surface-buoyancy-forcing-dominant zone. The threshold $\lambda_{s,c} = (R_{h,c}/R_{h,c}^*)^{3/2}$ indicates the transition between these wind-dominant zone and surface-buoyancy-forcing-dominant zone. These three thresholds are plotted normalized by their values at the lowest f/N_h : $R_{h,c0}$, $R_{h,c0}^*$ and $\lambda_{s,c0}$. Letters (a), (b), (c), (d), and (e) refer to the subfigures of Figure 3.

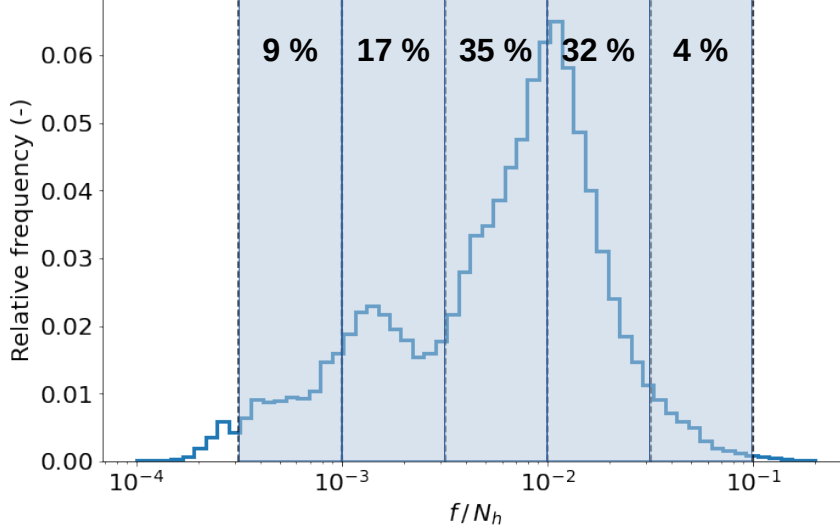


Figure 5. Relative frequency of the values of f/N_h for the 1D simulations at the global scale. The five slices used in Figure 3 are highlighted in light blue and the percentages of values falling in each of them are given.

ing values are reported in Figure 4 (following Equation 10, it could be calculated by $\lambda_{s,c} =$
 518 $(R_{h,c}/R_{h,c}^*)^{3/2}$). This dependency on f/N_h suggests that regions near the Equator are
 519 more likely to be in the wind-dominant regime, whereas high-latitude regions are more
 520 inclined toward a buoyancy-dominant regime.
 521

As previously observed, the $\lambda_s - R_h$ parameter space (Figure 2.a) exhibits high lev-
 522 els of significance even if the dimension f/N_h is not considered. This suggests that vari-
 523 ations of the f/N_h parameter are less important than variations of λ_s and R_h for pre-
 524 dicting a MLD evolution regime. Compared to the influence of f/N_h observed in Fig-
 525 ure 3, this behavior can be explained by the fact that the f/N_h distribution of the 1D
 526 simulations at the global scale is not uniform but dominated by values of $f/N_h \in [10^{-2.5}; 10^{-1.5}]$
 527 (cf Figure 5; and one can indeed see that demarcations of the Figure 2.a are close to the
 528 demarcations in Figure 3.c and Figure 3.d). Given the high statistical performance of
 529 the $\lambda_s - R_h$ parameter space, and because it is easier to work in two dimensions, we will
 530 focus solely on the $\lambda_s - R_h$ projection in the remainder of this article. The dimension
 531 f/N_h will only be considered if necessary to comprehend low significance levels.
 532

We conclude this section by noting that the statistical performance of the param-
 533 eter space is not specific to the TKE vertical mixing scheme (see Appendix A for a brief
 534

535 presentation of results with the KPP scheme). Additionally, for informative purposes,
 536 the density maps and associated joint Probability Density Functions (PDF) showing the
 537 density distribution of the values of λ_s , R_h , and f/N_h in the three 2D projections of the
 538 3D parameter space are given in Appendix B. This information can be useful when se-
 539 lecting relevant values of forcing and preconditioning conditions (u_*, B_0, N_h) in the con-
 540 text of parameter tuning (Souza et al., 2020; Wagner et al., 2023).

541 **3.2 Influence of the Horizontal Resolution on the MLD Evolution Regimes** 542 **for 3D Ocean Circulation Models**

543 Figure 6 displays the results of the 1D simulations, eORCA1, eORCA12, and eNATL60
 544 in the $\lambda_s - R_h$ parameter space for the global scale and in the Western Mediterranean
 545 region. Since all four simulations used the same 1D vertical scheme TKE+EVD, any vari-
 546 ations between the figures are attributed to the influence of lateral processes.

547 At the global scale, the main demarcation lines are consistent across the three sim-
 548 ulations. This observation suggests that, for predicting the MLD evolution, lateral pro-
 549 cesses are of second importance in comparison with the 1D processes presented via λ_s
 550 and R_h . However, this observation may not be locally valid. Extractions of the three same
 551 simulations in the Western Mediterranean, in addition to the eNATL60 simulation (which
 552 could not be considered at the global scale due to its basin-scale nature), reveal signif-
 553 icant variations across different resolutions. This indicates that the lateral processes play
 554 a substantial role in this region and cannot be neglected when compared to the 1D pro-
 555 cesses. Further details on these changes are provided in the following four paragraphs.

556 For $\lambda_s > -3$ and high values $R_h > 4000$ and $R_h^* > 4000$, the high resolution
 557 simulations ($1/12^\circ$ and $1/60^\circ$) exhibit some restratification points. High values of R_h and
 558 R_h^* indicate a stable MLD in terms of the 1D processes. The presence of restratification
 559 points suggests that the lateral processes, such as restratification by baroclinic instabil-
 560 ity at convective fronts or at mesoscale eddy fronts can become dominant and result in
 561 a MLD shoaling. In the same conditions ($\lambda_s > -3$; $R_h > 4000$; $R_h^* > 4000$), the 1°
 562 model behaves similarly to the 1D simulations, exhibiting a "stable" regime. This sug-
 563 gests that the coarse-resolution 1° model poorly resolves lateral processes of restratifi-
 564 cation.

565 For $\lambda_s > -3$ and low $R_h < 400$, going from 1D to 3D does not have a signifi-
 566 cant impact: the "strong deepening" regime is maintained in all four simulations. Low
 567 values of R_h indicate an unstable water column where the stratification is low compared
 568 to the wind forcing. The preservation of the "strong deepening" regime in all simulations
 569 suggests that for $R_h < 400$ the lateral processes of restratification cannot neutralize this
 570 instability and, therefore, play a secondary role.

571 The zone with $\lambda_s < -3$, dominated by surface buoyancy fluxes is a zone of restrat-
 572 ification or stable regimes for the 1D simulations. As mentioned earlier, we associated
 573 this behavior with a TKE-loss in the 1D TKE budget. Interestingly, this $\lambda_s < -3$ zone
 574 characterized by restratification or stable regimes is still observed in the 3D models. This
 575 implies that for a dominant surface-buoyancy restratifying flux ($\lambda_s < -3$), the lateral
 576 processes of TKE generation (such as an Ekman flow creating an equivalent destabiliz-
 577 ing wind-driven buoyancy flux, see for example Thomas & Lee, 2005) are of secondary
 578 importance compared to the processes of the 1D TKE budget.

579 The percentage of significant hexagons decreases when increasing the resolution:
 580 it is 97% in 1D, 88% at 1° , 84% at $1/12^\circ$ and 78% at $1/60^\circ$. Non-significant hexagons
 581 indicate that the predictive skill of the parameter space for the MLD evolution is ham-
 582 pered by the importance of lateral processes. Considering the parameter f/N_h does not
 583 improve the results (not shown). Other parameters, some of which are described in sec-
 584 tion 2.2, could improve the predictability. Investigating these higher-dimensional param-
 585 eter spaces could be a focus for future research.

586 **3.3 Impact of the GM Parameterization on a 1° Coarse-resolution Model**

587 In Figure 7, we plot the results of the eORCA1, eORCA1GM, and eNATL60 sim-
 588 ulations in the Western Mediterranean and the Labrador regions separately. We recall
 589 that eORCA1GM differs from eORCA1 solely due to the addition of the GM paramete-
 590 rization, designed to represent the adiabatic advective effect of unresolved mesoscale
 591 processes (Gent, 2011). Using eNATL60 as a reference helps evaluate how these mesoscale
 592 processes can influence the MLD evolution regimes in the parameter space. Therefore,
 593 comparing eORCA1GM and eNATL60 provides valuable insights into the impact of the
 594 GM parameterization, even though the GM parameterization was not designed to tackle
 595 the impact of the mesoscale processes in the mixed layer.

596 The impact of the GM parameterization is minimal in the Western Mediterranean
 597 region (Figure 7.a and Figure 7.b), although resolving the mesoscale processes was for
 598 instance expected to change the MLD evolution regimes from "stable" to "restratifica-
 599 tion" at high $R_h > 2000$ and high $R_h^* > 2000$ (Figure 7.a and Figure 7.c).

600 In the Labrador region, the GM parameterization has a visible impact where its
 601 main contribution is to generate a restratification zone at middle stability conditions ($200 <$
 602 $R_h < 2000$ in $-3 < \lambda_s < 2$; $200 < R_h^* < 2000$ in $\lambda_s > 2$) whereas it was before
 603 mainly a deepening zone (Figure 7.d and Figure 7.e). However, neither the stable zone
 604 ($R_h > 2000$ in $-3 < \lambda_s < 2$; $R_h^* > 2000$ in $\lambda_s > 2$) nor the strong deepening zone
 605 ($R_h < 200$ in $-3 < \lambda_s < 2$; $R_h^* < 200$ in $\lambda_s > 2$) are affected. These changes are not
 606 comparable with the effect of the mesoscale processes represented by the $1/60^\circ$ results
 607 (comparison Figure 7.d and Figure 7.f) for which, for instance, the restratification zone
 608 at middle stability conditions ($200 < R_h < 2000$ in $-3 < \lambda_s < 2$; $200 < R_h^* < 2000$ in
 609 $\lambda_s > 2$) is not observed.

610 Therefore, these two cases highlight that the impact of the mesoscale processes on
 611 the MLD evolution is not adequately captured by GM. To better characterize the im-
 612 pact of the GM parameterization as a function of the position in the parameter space,
 613 we can examine a proxy for its activation. The GM parameterization tends to flatten
 614 isopycnals by advecting tracers via eddy-induced velocities (Gent et al., 1995)

$$\begin{aligned} u_{GM} &= -\partial_z(\kappa_{GM}S_x) \\ v_{GM} &= -\partial_z(\kappa_{GM}S_y) \\ w_{GM} &= \partial_x(\kappa_{GM}S_x) + \partial_y(\kappa_{GM}S_y) \end{aligned} \tag{12}$$

615 with κ_{GM} the isopycnal thickness diffusivity, $S_x = -\partial_x\rho/\partial_z\rho$ the zonal isopycnal slope
 616 and $S_y = -\partial_y\rho/\partial_z\rho$ the meridional isopycnal slope.

617 We construct an index to quantify the magnitude of the GM rectification by con-
 618 sidering the horizontal transports integrated over the mixed layer $\gamma_x = \int_{-h}^0 -\partial_z(\kappa_{GM}S_x)dz$
 619 and $\gamma_y = \int_{-h}^0 -\partial_z(\kappa_{GM}S_y) dz$. The surface boundary condition imposes $w_{GM} = 0$.
 620 This condition is often satisfied by taking $\kappa_{GM}S_x = \kappa_{GM}S_y = 0$ at the surface. Thus
 621 $\gamma_x = \kappa_{GM}(z = -h)S_x(z = -h)$ and $\gamma_y = \kappa_{GM}(z = -h)S_y(z = -h)$: the integrated
 622 horizontal transports are proportional to the isopycnal slopes at the mixed layer base.
 623 The index is then constructed as the maximal isopycnal slope over the x and the y axes

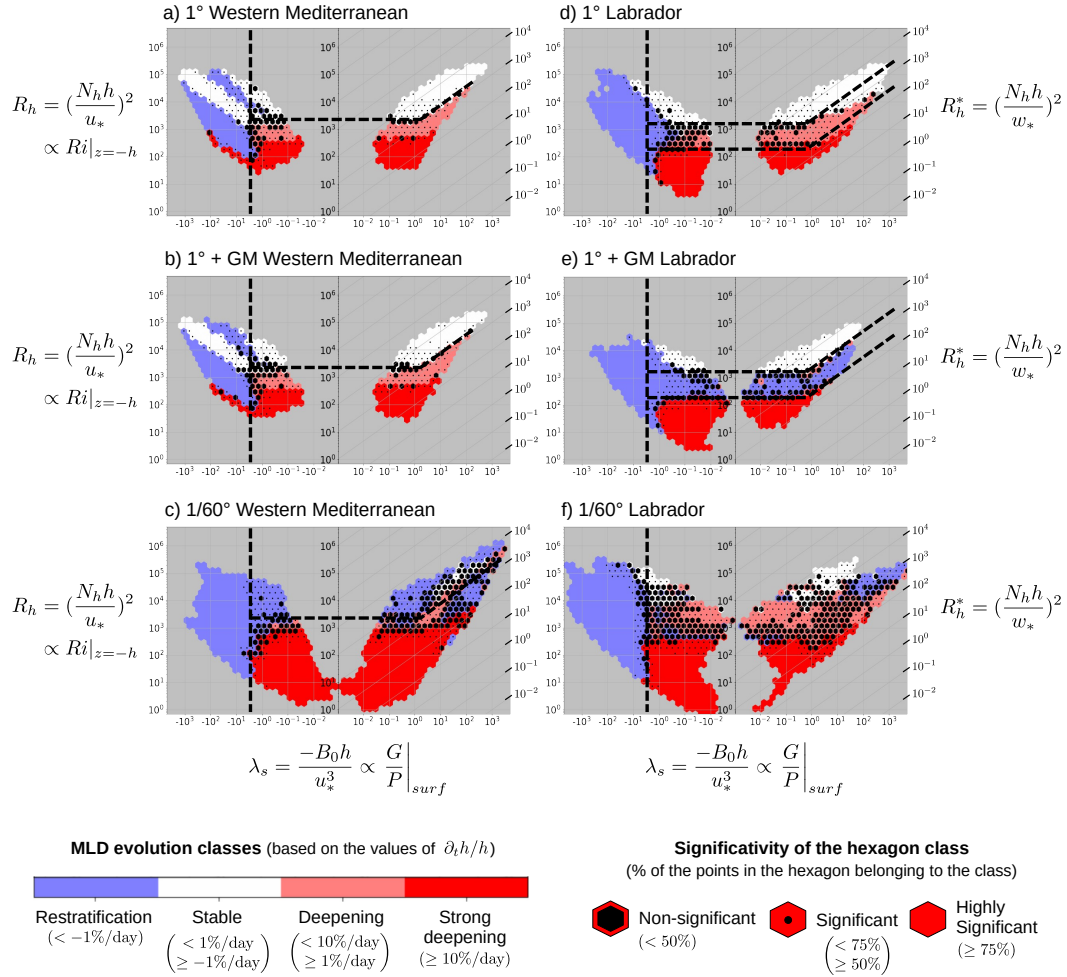


Figure 7. Results in the Western Mediterranean region of the (a) eORCA1, (b) eORCA1GM, and (c) eNATL60 simulations in the $\lambda_s - R_h$ parameter space. Figures (d), (e), and (f) are the same in the Labrador region. Dashed lines highlight important demarcations discussed in the text. Graphical conventions as in Figure 2.

$$\begin{aligned}
 S_h &= \max(|S_x(z = -h)|; |S_y(z = -h)|) \\
 &= \max\left(\left|\frac{\partial_x \rho(z = -h)}{\partial_z \rho(z = -h)}\right|; \left|\frac{\partial_y \rho(z = -h)}{\partial_z \rho(z = -h)}\right|\right)
 \end{aligned} \tag{13}$$

624 with $\partial_z \rho(z = -h)$ calculated over a distance $0.1h$ below the mixed layer: $\partial_z \rho(z = -h) =$
 625 $\frac{\rho(z = -1.1h) - \rho(z = -h)}{0.1h}$.

626 The regions where the GM parameterization has a notable impact are character-
 627 ized by high values of S_h (Figure 8.a and Figure 8.e; see also the comparison between
 628 Figures 8.b and 8.d, and Figures 8.f and 8.h). In the Western Mediterranean region, we
 629 can define a threshold $S_h = 0.5$ m/km below which the GM parameterization is expected
 630 to have negligible impact. Filtering the eORCA1GM results by the condition $S_h < 0.5$ m/km,
 631 yields results comparable to the results of the eORCA1 simulation (comparison Figures
 632 8.c and 8.d, and Figures 8.g and 8.h). This confirms that the observed impacts of the
 633 GM parameterization can be understood through the values of S_h . Hence, this number
 634 is an additional dimensionless number that could be considered when R_h and λ_s alone
 635 do not provide robust predictions. In future studies, exploring projections into param-
 636 eter spaces (λ_s, S_h) or (R_h, S_h) could be promising avenues.

637 4 Conclusions and Discussion

638 This study introduces a three-dimensional parameter space designed to facilitate
 639 the analysis and the intercomparison of the ocean MLD evolution between numerical mod-
 640 els. The parameter space consists of three dimensionless numbers R_h , λ_s and f/N_h de-
 641 rived through dimensional analysis: λ_s evaluates the relative influence of the buoyancy
 642 forcing and the wind forcing for producing/destroying TKE in the surface layer, R_h is
 643 the Richardson number describing the competition between the stabilizing effect of the
 644 pycnocline stratification and the destabilizing impact of the wind-induced shear. Finally,
 645 f/N_h evaluates the influence of the Earth's rotation.

646 The $\lambda_s - R_h - f/N_h$ parameter space was first evaluated in the context of 1D sim-
 647 ulations. Four MLD evolution regimes were defined based on the value of the relative
 648 MLD change $\partial_t h/h$: "Restratification", "Stable", "Deepening" and "Strong Deepening".
 649 We showed that the influence of rotation tends to stabilize the water column by reduc-
 650 ing the effective forcings of the wind and the surface buoyancy flux. This reduction is
 651 even more pronounced on the wind forcing and consequently, MLD deepening in high

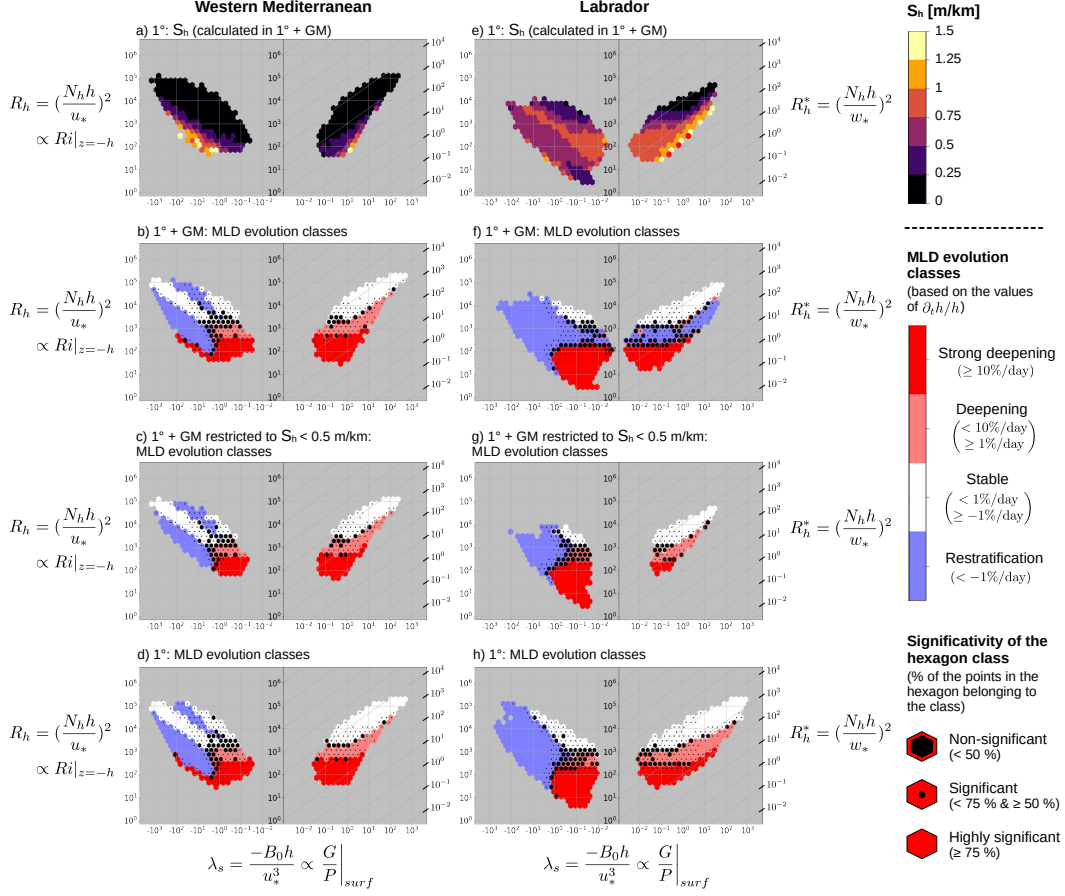


Figure 8. Results in the Western Mediterranean region in the $\lambda_s - R_h$ parameter space of (a) S_h in eORCA1, (b) MLD evolution classes in eORCA1GM, (c) MLD evolution classes in eORCA1GM restricted to $S_h < 0.5$ m/km and (d) MLD evolution classes in eORCA1. Figures (d), (e), and (f) are the same in the Labrador region. The slope S_h of the isopycnets at the MLD is expressed in m/km. Values that exceeded 1.5 m/km are represented in red. Graphical conventions as in Figure 2.

652 latitude regions is more inclined to be dominated by the surface buoyancy forcing whereas
 653 the Equator is more inclined to be wind-dominant. This can be related to the numer-
 654 ous studies that assess the relative importance of wind and surface buoyancy forcings
 655 in different regions (Dong et al., 2007; Sallée et al., 2010; Downes et al., 2011; Holte et
 656 al., 2012; Sallée et al., 2021; Gao et al., 2023). For example, Sallée et al. (2010) stated
 657 that the surface buoyancy forcing in the Southern Ocean (high latitude) dominates the
 658 wind forcing by one order of magnitude. Our study, which shows the dependence on f/N_h
 659 of the $\lambda_{s,c}$ threshold between the two regimes, provides a new practical way of determin-
 660 ing the relative importance of surface buoyancy flux versus wind.

661 The influence of the f/N_h parameter is less important than the λ_s and R_h param-
 662 eters for predicting the MLD evolution. The two-dimensional parameter space $\lambda_s - R_h$
 663 indeed exhibits high statistical performances with, in 96 % of the cases, a pair (λ_s, R_h)
 664 that corresponds to a unique MLD evolution regime. In other words, instead of exam-
 665 ining all the preconditioning and forcing conditions, one can just calculate the two di-
 666 mensionless numbers λ_s and R_h for predicting the MLD evolution regimes. Also, the MLD
 667 evolution regimes appear in well-separated zones. This spatial coherence of regimes in
 668 this parameter space allows us to define thresholds on (λ_s, R_h) to predict MLD evolu-
 669 tion regimes.

670 The thresholds of the $\lambda_s - R_h$ parameter space were described in the context of 1D
 671 simulations. The criterion $\lambda_s < -3$ indicates stable or restratification regimes and is
 672 valid for all f/N_h values. The wind-dominant zone $-3 < \lambda_s < 0.2$ is characterized
 673 by transitions according to R_h -only thresholds. In the buoyancy-flux-dominant zone $\lambda_s >$
 674 0.2 , transitions between regimes can be seen as thresholds on $R_h^* = (N_h h/w_*)^2$, the Richard-
 675 son number associated with the destabilizing buoyancy flux. This threshold at $\lambda_s \approx 0.2$
 676 between the wind-dominant and the surface-buoyancy-flux-dominant zones is the one for
 677 the global scale, which is representative of f/N_h values in $[10^{-2.5}; 10^{-1.5}]$, and must be
 678 adjusted for different values of f/N_h .

679 Two applications of the parameter space were presented and we show how it may
 680 be used with realistic ocean models. In the first application, we intercompare ocean sim-
 681 ulations at different horizontal resolutions to evaluate the effect of lateral processes on
 682 the MLD evolution. We showed that lateral processes play a secondary role for low val-
 683 ues of R_h and R_h^* : the stratification effect is weak compared to the forcing u_* or w_* and

684 the "strong deepening" regime can be predicted without considering lateral processes.
 685 When the water column is stable with respect to 1D processes (large values of R_h and
 686 R_h^*), we showed that the lateral restratification processes become dominant in the high-
 687 resolution simulations ($1/12^\circ$ and $1/60^\circ$). These lateral processes may for example in-
 688 clude the restratification by baroclinic instability at convective fronts or at mesoscale eddy
 689 fronts. However, the 1° model behaves as the 1D model, suggesting that the lateral pro-
 690 cesses of restratification are not resolved at this resolution without GM. Finally, in the
 691 high-resolution simulations ($1/12^\circ$ and $1/60^\circ$), the non-significant zones at mid values
 692 of R_h and R_h^* indicate that the lateral processes are dominant and that other dimension-
 693 less numbers could be considered for predicting the MLD evolution regime.

694 The second application shows that the adiabatic advective effect of the mesoscale
 695 processes parameterized by GM parameterization does not capture the full impact of un-
 696 resolved mesoscale processes on the MLD evolution regimes in a coarse-resolution 1° model.
 697 In this context, we introduced the dimensionless number S_h which is the maximal isopy-
 698 cnal slope at the mixed layer base. This slope is one of the other dimensionless numbers
 699 that could be considered when the two (R_h, λ_s) are not sufficient for obtaining robust
 700 predictions. Particularly, projections into the parameter space (λ_s, S_h) or (R_h, S_h) could
 701 constitute some developments for future works.

702 The two applications presented in this study are not exhaustive. We decided to fo-
 703 cus here on the use of the parameter space for model sensitivity studies. Future work
 704 could use the parameter space for comparing the behaviors of different vertical mixing
 705 schemes (KPP, TKE, GLS) and for comparing coupled and forced models. The infor-
 706 mation of the joint PDF of the three 2D projections of the 3D parameter space, given
 707 in Appendix B could also be used for choosing relevant values of forcing and precondi-
 708 tioning conditions (u_*, B_0, N_h) in the context of parameter tuning (Souza et al., 2020;
 709 Wagner et al., 2023). Beyond these direct applications, an interesting extension of the
 710 approach would be to evaluate the performance of the parameter space with LES data
 711 and observations. For the observations, ARGO floats could for example be used. They
 712 give profiles over 10-day periods and the parameter space will need to be assessed with
 713 this new period. Fluxes between the ocean and the atmosphere could for example be ob-
 714 tained through the European Centre for Medium-Range Weather Forecasts (ECMWF)
 715 open data. For the LES, it would be possible to keep the 1-day period developed in this
 716 study or to try also with shorter or longer periods. In short, if the statistical performance

717 is still obtained in these contexts, the parameter space could become an informative tool
718 for calibrating the mixing schemes using LES or observational data as a truth.

719 **Appendix A Analysis with the KPP Vertical Mixing Scheme**

720 To verify if the statistical performance of the parameter space is sensitive to the
721 vertical mixing scheme, we performed the same collection of 1D water column simula-
722 tions described in section 2.7 but with a KPP scheme instead of a TKE + EVD scheme.
723 Figure A1 presents the results of these simulations with the same conventions as Fig-
724 ure 2. Again, the $\lambda_s - N_h$ parameter space performs well with 96 % of significant hexagons,
725 and spatial coherence of well-delimited zones is still obtained. The demarcation thresh-
726 olds (represented by dashed lines) could again be discussed. In short, all the diagnos-
727 tics we have done previously could have been done with simulations based on the KPP
728 scheme as well, and future research could focus on analyzing the difference in behaviors
729 between the TKE + EVD scheme and the KPP mixing scheme.

730 **Appendix B Joint PDF of Three 2D Projections of the 3D Parameter Space**

731 We plot in Figure B1 the density maps in the three 2D projections of the 3D pa-
732 rameter space and the contours of the associated joint PDF, calculated with the 1D sim-
733 ulations outputs at the global scale through the Python functions provided by Q. Li et
734 al. (2019). These contours enclose 30 % (black), 60 % (blue), 90 % (green), and 99 % (yel-
735 low) of all instances centered at the highest PDF.

736 **Appendix C Open Research**

737 All the codes used for the study are available through the following GitHub reposi-
738 tory: https://github.com/legaya/James2023_ParameterSpace/. It contains the Jupyter
739 Notebook used for performing the 1D simulations and all the analyses, the 1D model de-
740 scribed in section 2.1 as a Fortran Module "scm_oce.so", and the Fortran codes needed
741 for generating this module. The eORCA1, eORCA1GM, eORCA12, and eNATL60 sim-
742 ulations outputs needed for realizing the figures are available as netCDF files and "npz"
743 archives via the following DOI: <https://doi.org/10.5281/zenodo.10423178>.

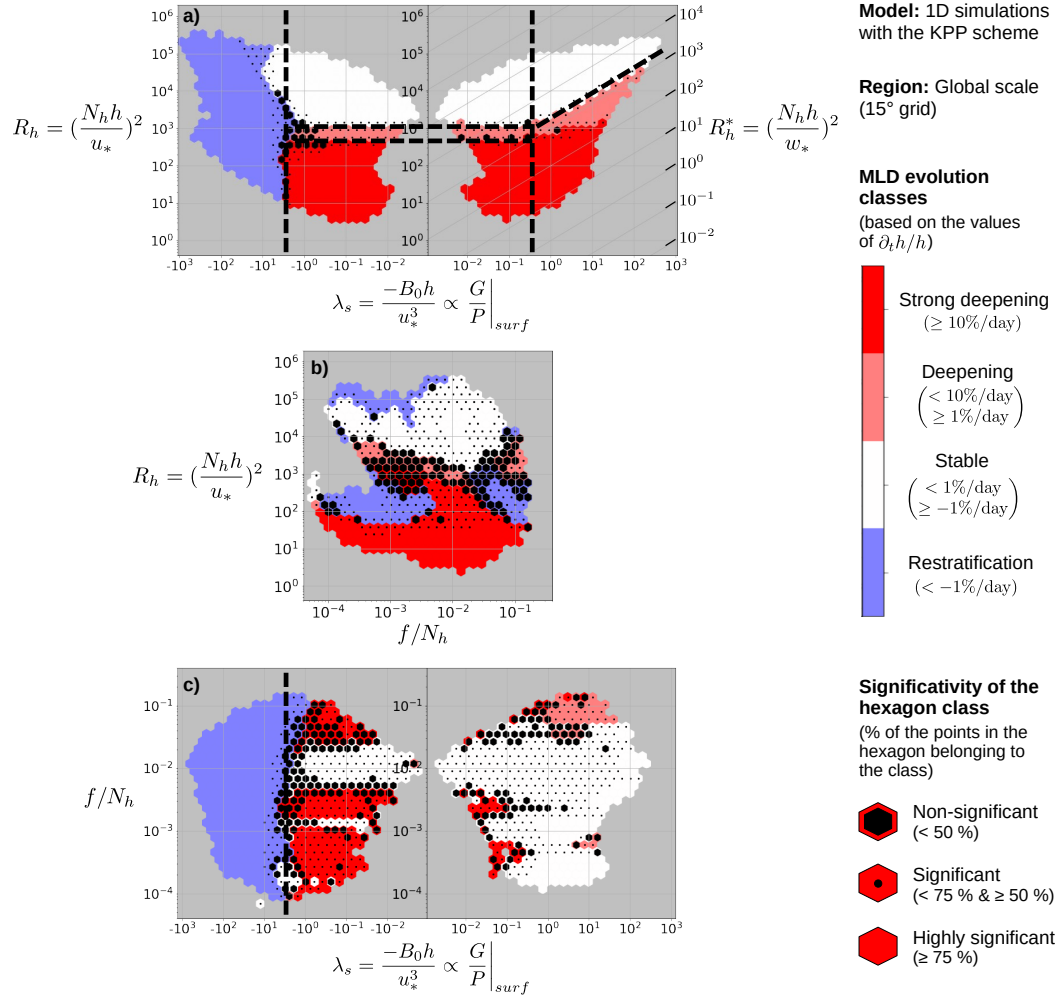


Figure A1. Same as Figure 2 but with 1D simulations using a KPP vertical mixing scheme instead of a TKE + EVD scheme.

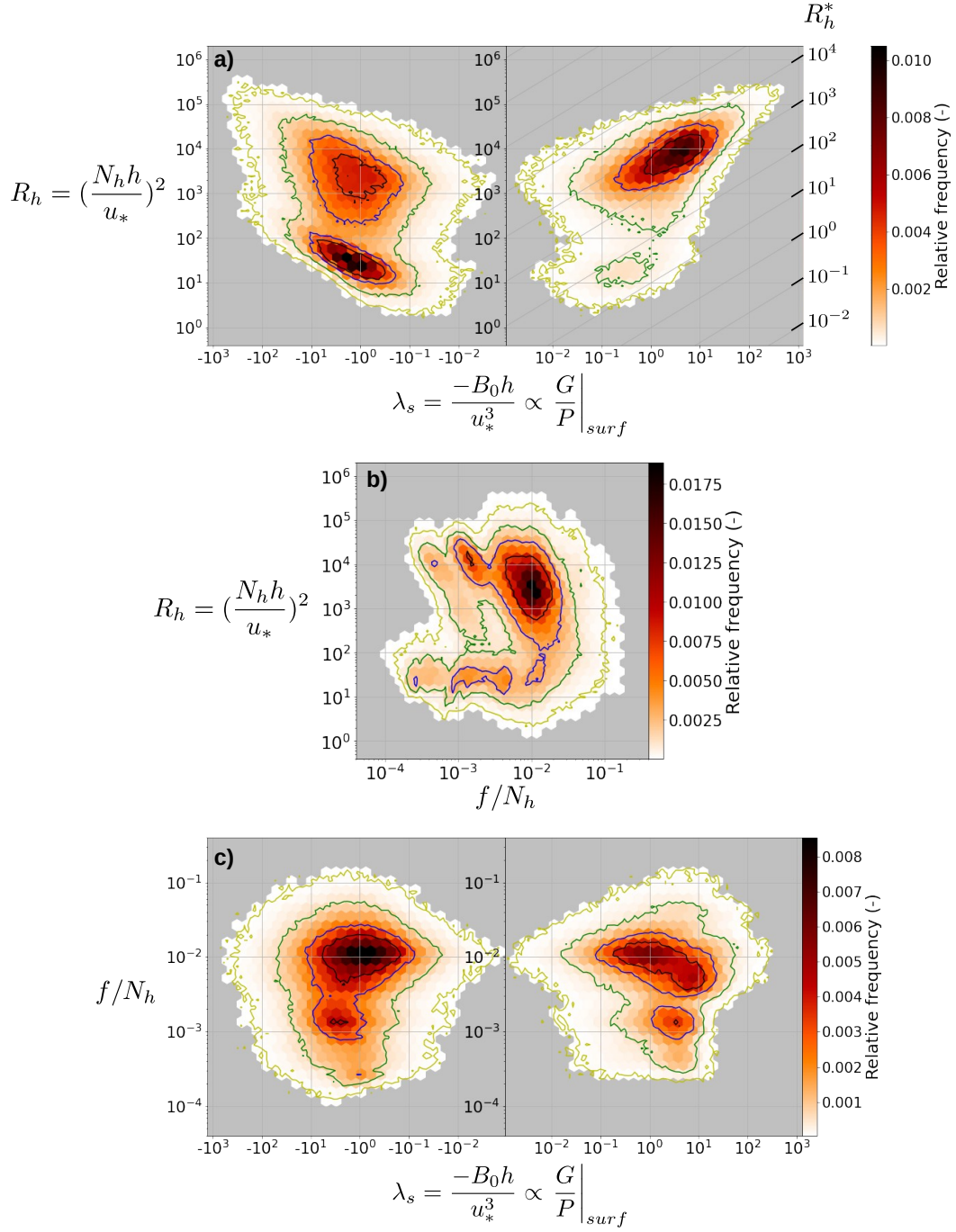


Figure B1. Density maps of the 1D simulations at the global scale for the a) $\lambda_s - R_h$, b) $f/N_h - R_h$ and c) $\lambda_s - f/N_h$ parameter space. The contours of the associated joint PDF are superimposed. These contours enclose 30% (black), 60% (blue), 90% (green), and 99% (yellow) of all instances centered at the highest PDF.

744 Acknowledgments

745 We thank Florian Lemarié for providing the 1D code, and Aurélie Albert for the extrac-
 746 tions of the eNATL60 and eORCA12 simulations. All the computations presented in this
 747 paper were performed using the GRICAD infrastructure ([https://gricad.univ-grenoble-](https://gricad.univ-grenoble-alpes.fr)
 748 [alpes.fr](https://gricad.univ-grenoble-alpes.fr)), which is supported by Grenoble research communities. Thierry Penduff is sup-
 749 ported by the MixED Layer hETerogeneity (MEDLEY) project which has received fund-
 750 ing from the Joint Programming Initiative (JPI) Climate and JPI Oceans programs un-
 751 der the 2019 joint call, managed by the French Agence Nationale de la Recherche (con-
 752 tract no. 19-JPOC-0001-01).

753 References

- 754 Aurnou, J. M., Horn, S., & Julien, K. (2020). Connections between nonrotating,
 755 slowly rotating, and rapidly rotating turbulent convection transport scalings.
 756 *Phys. Rev. Res.*, *2*(4), 043115. doi: 10.1103/PhysRevResearch.2.043115
- 757 Banks, H. T., & Gregory, J. M. (2006). Mechanisms of ocean heat uptake in a
 758 coupled climate model and the implications for tracer based predictions
 759 of ocean heat uptake. *Geophysical Research Letters*, *33*(7), L07608. doi:
 760 10.1029/2005GL025352
- 761 Belcher, S. E., Grant, A. L. M., Hanley, K. E., Fox-Kemper, B., Van Roekel, L.,
 762 Sullivan, P. P., ... Polton, J. A. (2012). A global perspective on Langmuir
 763 turbulence in the ocean surface boundary layer: FRONTIER. *Geophysical*
 764 *Research Letters*, *39*(18). doi: 10.1029/2012GL052932
- 765 Bernardello, R., Marinov, I., Palter, J. B., Galbraith, E. D., & Sarmiento, J. L.
 766 (2014). Impact of Weddell Sea deep convection on natural and anthropogenic
 767 carbon in a climate model. *Geophysical Research Letters*, *41*(20), 7262–7269.
 768 doi: 10.1002/2014GL061313
- 769 Boccaletti, G., Ferrari, R., & Fox-Kemper, B. (2007). Mixed Layer Instabilities and
 770 Restratification. *Journal of Physical Oceanography*, *37*(9), 2228–2250. doi: 10
 771 .1175/JPO3101.1
- 772 Bouillaut, V., Lepot, S., Aumaître, S., & Gallet, B. (2019). Transition to the ul-
 773 timate regime in a radiatively driven convection experiment. *J. Fluid Mech.*,
 774 *861*, R5. doi: 10.1017/jfm.2018.972
- 775 Brodeau, L., Le Sommer, J., & Albert, A. (2020). *ocean-next/eNATL60: Material*

- 776 *describing the set-up and the assessment of NEMO-eNATL60 simulations.*
777 Zenodo. doi: 10.5281/ZENODO.4032732
- 778 Burchard, H., & Bolding, K. (2001). Comparative Analysis of Four Second-Moment
779 Turbulence Closure Models for the Oceanic Mixed Layer. *Journal of Physi-*
780 *cal Oceanography*, 31(8), 1943–1968. doi: 10.1175/1520-0485(2001)031<1943:
781 CAOFSM>2.0.CO;2
- 782 Damerell, G. M., Heywood, K. J., Calvert, D., Grant, A. L., Bell, M. J., & Belcher,
783 S. E. (2020). A comparison of five surface mixed layer models with a year of
784 observations in the North Atlantic. *Progress in Oceanography*, 187, 102316.
785 doi: 10.1016/j.pocean.2020.102316
- 786 de Boyer Montégut, C., Madec, G., Fischer, A. S., Lazar, A., & Iudicone, D. (2004).
787 Mixed layer depth over the global ocean: An examination of profile data and a
788 profile-based climatology. *Journal of Geophysical Research*, 109(C12), C12003.
789 doi: 10.1029/2004JC002378
- 790 Dee, D. P., Uppala, S. M., Simmons, A. J., Berrisford, P., Poli, P., Kobayashi, S., ...
791 Vitart, F. (2011). The ERA-Interim reanalysis: configuration and performance
792 of the data assimilation system. *Quarterly Journal of the Royal Meteorological*
793 *Society*, 137(656), 553–597. doi: 10.1002/qj.828
- 794 Deremble, B. (2016). Convective plumes in rotating systems. *J. Fluid Mech.*, 799,
795 27–55. doi: 10.1017/jfm.2016.348
- 796 Dong, S., Gille, S. T., & Sprintall, J. (2007). An Assessment of the Southern Ocean
797 Mixed Layer Heat Budget. *Journal of Climate*, 20(17), 4425–4442. doi: 10
798 .1175/JCLI4259.1
- 799 Downes, S. M., Budnick, A. S., Sarmiento, J. L., & Farneti, R. (2011). Impacts of
800 wind stress on the Antarctic Circumpolar Current fronts and associated sub-
801 duction: ACC FRONTS AND SUBDUCTION. *Geophysical Research Letters*,
802 38(11), n/a–n/a. doi: 10.1029/2011GL047668
- 803 Ekman, V. W. (1905). On the influence of earth’s rotation on ocean currents. *Ark.*
804 *Math. Astron. Phys.*, 2, 1–53.
- 805 Fearon, G., Herbette, S., Veitch, J., Cambon, G., Lucas, A. J., Lemarié, F., & Vichi,
806 M. (2020). Enhanced vertical mixing in coastal upwelling systems driven by
807 diurnal-inertial resonance: Numerical experiments. *Journal of Geophysical*
808 *Research: Oceans*, 125(9), e2020JC016208. doi: 10.1029/2020JC016208

- 809 Fofonoff, N. P., & Millard Jr, R. (1983). *Algorithms for the computation of funda-*
 810 *mental properties of seawater.* (Tech. Rep.). UNESCO. doi: 10.25607/OBP
 811 -1450
- 812 Fox-Kemper, B., Ferrari, R., & Hallberg, R. (2007). Parameterization of Mixed
 813 Layer Eddies. I: Theory and Diagnosis. *Journal of Physical Oceanography.* doi:
 814 10.1175/2007JPO3792.1
- 815 Gao, Y., Kamenkovich, I., & Perlin, N. (2023). Origins of mesoscale mixed-layer
 816 depth variability in the Southern Ocean. *Ocean Science*, *19*(3), 615–627. doi:
 817 10.5194/os-19-615-2023
- 818 Gaspar, P. (1988). Modeling the seasonal cycle of the upper ocean. *Journal of Phys-*
 819 *ical Oceanography*, *18*(2), 161 - 180. doi: 10.1175/1520-0485(1988)018<0161:
 820 MTSCOT>2.0.CO;2
- 821 Gaspar, P., Grégoris, Y., & Lefevre, J.-M. (1990). A simple eddy kinetic energy
 822 model for simulations of the oceanic vertical mixing: Tests at station Papa and
 823 long-term upper ocean study site. *Journal of Geophysical Research*, *95*(C9),
 824 16179. doi: 10.1029/JC095iC09p16179
- 825 Gent, P. R. (2011). The Gent–McWilliams parameterization: 20/20 hindsight.
 826 *Ocean Modelling*, *39*(1-2), 2–9. doi: 10.1016/j.ocemod.2010.08.002
- 827 Gent, P. R., & McWilliams, J. C. (1990). Isopycnal mixing in ocean circulation
 828 models. *Journal of Physical Oceanography*, *20*(1), 150 - 155. doi: 10.1175/1520
 829 -0485(1990)020<0150:IMIOCM>2.0.CO;2
- 830 Gent, P. R., Willebrand, J., McDougall, T. J., & McWilliams, J. C. (1995). Param-
 831 eterizing Eddy-Induced Tracer Transports in Ocean Circulation Models. *Jour-*
 832 *nal of Physical Oceanography*, *25*(4), 463–474. doi: 10.1175/1520-0485(1995)
 833 025<0463:PEITTI>2.0.CO;2
- 834 Giordani, H., Bourdallé-Badie, R., & Madec, G. (2020). An Eddy-Diffusivity Mass-
 835 Flux Parameterization for Modeling Oceanic Convection. *Journal of Advances*
 836 *in Modeling Earth Systems*, *12*(9). doi: 10.1029/2020MS002078
- 837 Griffies, S. M., Danabasoglu, G., Durack, P. J., Adcroft, A. J., Balaji, V., Böning,
 838 C. W., ... Yeager, S. G. (2016). OMIP contribution to CMIP6: experimental
 839 and diagnostic protocol for the physical component of the Ocean Model Inter-
 840 comparison Project. *Geoscientific Model Development*, *9*(9), 3231–3296. doi:
 841 10.5194/gmd-9-3231-2016

- 842 Gutjahr, O., Brüggemann, N., Haak, H., Jungclaus, J. H., Putrasahan, D. A.,
 843 Lohmann, K., & von Storch, J.-S. (2021). Comparison of ocean ver-
 844 tical mixing schemes in the Max Planck Institute Earth System Model
 845 (MPI-ESM1.2). *Geoscientific Model Development*, *14*(5), 2317–2349. doi:
 846 10.5194/gmd-14-2317-2021
- 847 Hanjalić, K., & Launder, B. E. (1972). A Reynolds stress model of turbulence and
 848 its application to thin shear flows. *Journal of Fluid Mechanics*, *52*(4), 609–638.
 849 doi: 10.1017/S002211207200268X
- 850 Heuzé, C. (2017). North Atlantic deep water formation and AMOC in CMIP5 mod-
 851 els. *Ocean Science*, *13*(4), 609–622. doi: 10.5194/os-13-609-2017
- 852 Holte, J. W., Talley, L. D., Chereskin, T. K., & Sloyan, B. M. (2012). The role of
 853 air-sea fluxes in Subantarctic Mode Water formation. *Journal of Geophysical*
 854 *Research: Oceans*, *117*(C3), 2011JC007798. doi: 10.1029/2011JC007798
- 855 Koenigk, T., Fuentes-Franco, R., Meccia, V. L., Gutjahr, O., Jackson, L. C., New,
 856 A. L., ... Sein, D. V. (2021). Deep mixed ocean volume in the Labrador
 857 Sea in HighResMIP models. *Climate Dynamics*, *57*(7-8), 1895–1918. doi:
 858 10.1007/s00382-021-05785-x
- 859 Kraus, E. B., & Turner, J. S. (1967). A one-dimensional model of the seasonal ther-
 860 mocline II. *The general theory and its consequences. Tellus*, *19*(1), 98–106. doi:
 861 10.1111/j.2153-3490.1967.tb01462.x
- 862 Kuhlbrodt, T., Griesel, A., Montoya, M., Levermann, A., Hofmann, M., & Rahm-
 863 storf, S. (2007). On the driving processes of the Atlantic meridional
 864 overturning circulation. *Reviews of Geophysics*, *45*(2), RG2001. doi:
 865 10.1029/2004RG000166
- 866 Large, W. G., McWilliams, J. C., & Doney, S. C. (1994). Oceanic vertical mixing: A
 867 review and a model with a nonlocal boundary layer parameterization. *Reviews*
 868 *of Geophysics*, *32*(4), 363. doi: 10.1029/94RG01872
- 869 Lazar, A., Madec, G., & Delecluse, P. (1999). The deep interior downwelling,
 870 the veronis effect, and mesoscale tracer transport parameterizations in
 871 an ogcm. *Journal of Physical Oceanography*, *29*(11), 2945 - 2961. doi:
 872 [https://doi.org/10.1175/1520-0485\(1999\)029<2945:TDIDTV>2.0.CO;2](https://doi.org/10.1175/1520-0485(1999)029<2945:TDIDTV>2.0.CO;2)
- 873 Lellouche, J.-M., Chassignet, E., Bourdallé-Badie, R., Garric, G., Melet, A.,
 874 Drévillon, M., ... Le Traon, P.-Y. (2021). The Copernicus Global 1/12°

- 875 Oceanic and Sea Ice GLORYS12 Reanalysis. *Frontiers in Earth Science*, 9,
876 698876. doi: 10.3389/feart.2021.698876
- 877 Li, M., & Garrett, C. (1993). Cell merging and the jet/downwelling ratio in Lang-
878 muir circulation. *Journal of Marine Research*, 51(4), 737–769. doi: 10.1175/
879 1520-0485(1997)027<0121:MLDDTL>2.0.CO;2
- 880 Li, Q., Reichl, B. G., Fox-Kemper, B., Adcroft, A. J., Belcher, S. E., Danabasoglu,
881 G., . . . Zheng, Z. (2019). Comparing Ocean Surface Boundary Vertical Mixing
882 Schemes Including Langmuir Turbulence. *Journal of Advances in Modeling*
883 *Earth Systems*, 11(11), 3545–3592. doi: 10.1029/2019MS001810
- 884 Lévy, M., Mémerly, L., & Madec, G. (1998). The onset of a bloom after deep winter
885 convection in the northwestern Mediterranean sea: mesoscale process study
886 with a primitive equation model. *Journal of Marine Systems*, 16(1-2), 7–21.
887 doi: 10.1016/S0924-7963(97)00097-3
- 888 Mack, S. A., & Schoeberlein, H. C. (2004). Richardson Number and Ocean Mixing:
889 Towed Chain Observations. *Journal of Physical Oceanography*, 34(4), 736–754.
890 doi: 10.1175/1520-0485(2004)034<0736:RNAOMT>2.0.CO;2
- 891 Madec, G., Bourdallé-Badie, R., Chanut, J., Clementi, E., Coward, A., Ethé, C., . . .
892 Moulin, A. (2022). *NEMO ocean engine*. (Publisher: Zenodo Version Number:
893 v4.2) doi: 10.5281/ZENODO.1464816
- 894 Marshall, J., & Schott, F. (1999). Open-ocean convection: Observations, theory, and
895 models. *Reviews of geophysics*, 37(1), 1–64. doi: 10.1029/98RG02739
- 896 Mellor, G. L. (1973). Analytic prediction of the properties of stratified planetary
897 surface layers. *Journal of Atmospheric Sciences*, 30(6), 1061 - 1069. doi: 10
898 .1175/1520-0469(1973)030<1061:APOTPO>2.0.CO;2
- 899 Mellor, G. L., & Durbin, P. A. (1975). The structure and dynamics of the ocean sur-
900 face mixed layer. *Journal of Physical Oceanography*, 5, 718-728. doi: 10.1175/
901 1520-0485(1975)005<0718:TSADOT>2.0.CO;2
- 902 Mellor, G. L., & Yamada, T. (1974). A hierarchy of turbulence closure models for
903 planetary boundary layers. *Journal of Atmospheric Sciences*, 31(7), 1791 -
904 1806. doi: 10.1175/1520-0469(1974)031<1791:AHOTCM>2.0.CO;2
- 905 Mellor, G. L., & Yamada, T. (1982). Development of a turbulence closure model for
906 geophysical fluid problems. *Reviews of Geophysics*, 20(4), 851. doi: 10.1029/
907 RG020i004p00851

- 908 Obukhov, A. M. (1971). Turbulence in an atmosphere with a non-uniform tempera-
 909 ture. *Boundary-Layer Meteorology*, *2*(1), 7–29. doi: 10.1007/BF00718085
- 910 Pollard, R. T., Rhines, P. B., & Thompson, R. O. R. Y. (1973). The deepening of
 911 the wind-mixed layer. *Geophysical Fluid Dynamics*, *4*(4), 381–404. doi: 10
 912 .1080/03091927208236105
- 913 Price, J. F. (1979). On the scaling of stress-driven entrainment experiments. *Journal*
 914 *of Fluid Mechanics*, *90*(3), 509–529. doi: 10.1017/S0022112079002366
- 915 Price, J. F., Weller, R. A., & Pinkel, R. (1986). Diurnal cycling: Observa-
 916 tions and models of the upper ocean response to diurnal heating, cooling,
 917 and wind mixing. *Journal of Geophysical Research*, *91*(C7), 8411. doi:
 918 10.1029/JC091iC07p08411
- 919 Reichl, B. G., & Hallberg, R. (2018). A simplified energetics based planetary bound-
 920 ary layer (ePBL) approach for ocean climate simulations. *Ocean Modelling*,
 921 *132*, 112–129. doi: 10.1016/j.ocemod.2018.10.004
- 922 Rodi, W. (1987). Examples of calculation methods for flow and mixing in strat-
 923 ified fluids. *Journal of Geophysical Research*, *92*(C5), 5305. doi: 10.1029/
 924 JC092iC05p05305
- 925 Sallée, J.-B., Pellichero, V., Akhoudas, C., Pauthenet, E., Vignes, L., Schmidtko,
 926 S., ... Kuusela, M. (2021). Summertime increases in upper-ocean strat-
 927 ification and mixed-layer depth. *Nature*, *591*(7851), 592–598. doi:
 928 10.1038/s41586-021-03303-x
- 929 Sallée, J. B., Speer, K. G., & Rintoul, S. R. (2010). Zonally asymmetric response of
 930 the Southern Ocean mixed-layer depth to the Southern Annular Mode. *Nature*
 931 *Geoscience*, *3*(4), 273–279. doi: 10.1038/ngeo812
- 932 Schulzweida, U. (2023). *Cdo user guide*. Zenodo. doi: 10.5281/zenodo.10020800
- 933 Shy, S. (1995). Mixing dynamics of jet interaction with a sharp density interface.
 934 *Experimental Thermal and Fluid Science*, *10*(3), 355–369. doi: 10.1016/0894
 935 -1777(94)00095-P
- 936 Simpson, J. H., & Hunter, J. R. (1974). Fronts in the Irish sea. *Nature*, *250*(5465),
 937 404–406. doi: 10.1038/250404a0
- 938 Souza, A. N., Wagner, G. L., Ramadhan, A., Allen, B., Churavy, V., Schloss, J.,
 939 ... Ferrari, R. (2020). Uncertainty Quantification of Ocean Parameteriza-
 940 tions: Application to the K-Profile-Parameterization for Penetrative Con-

- 941 vection. *Journal of Advances in Modeling Earth Systems*, 12(12). doi:
 942 10.1029/2020MS002108
- 943 Speer, K. G., & Marshall, J. (1995). The growth of convective plumes at seafloor hot
 944 springs. *J. Mar. Res.*, 53(6), 1025–1057. doi: 10.1357/0022240953212972
- 945 Stull, R. B. (Ed.). (1988). *An Introduction to Boundary Layer Meteorology*. Dor-
 946 drecht: Springer Netherlands. doi: 10.1007/978-94-009-3027-8
- 947 Sverdrup, H. (1953). On conditions for the vernal blooming of phytoplankton. *J.*
 948 *Cons. Int. Explor. Mer.*, 18(3), 287–295. doi: 10.1093/icesjms/18.3.287
- 949 Sérazin, G., Tréguier, A. M., & De Boyer Montégut, C. (2023). A seasonal climatol-
 950 ogy of the upper ocean pycnocline. *Frontiers in Marine Science*, 10, 1120112.
 951 doi: 10.3389/fmars.2023.1120112
- 952 Taylor, J. R., & Ferrari, R. (2011). Shutdown of turbulent convection as a new crite-
 953 rion for the onset of spring phytoplankton blooms. *Limnology and Oceanogra-*
 954 *phy*, 56(6), 2293–2307. doi: 10.4319/lo.2011.56.6.2293
- 955 Thangam, S., Abid, R., & Speziale, C. G. (1992). Application of a new K-tau model
 956 to near wall turbulent flows. *AIAA Journal*, 30(2), 552–554. doi: 10.2514/3
 957 .10952
- 958 Thomas, L. N., & Lee, C. M. (2005). Intensification of Ocean Fronts by Down-Front
 959 Winds. *Journal of Physical Oceanography*, 35(6), 1086–1102. doi: 10.1175/
 960 JPO2737.1
- 961 Treguier, A. M., De Boyer Montégut, C., Bozec, A., Chassignet, E. P., Fox-
 962 Kemper, B., McC. Hogg, A., ... Yeager, S. (2023). The mixed-layer depth
 963 in the Ocean Model Intercomparison Project (OMIP): impact of resolving
 964 mesoscale eddies. *Geoscientific Model Development*, 16(13), 3849–3872. doi:
 965 10.5194/gmd-16-3849-2023
- 966 Tsujino, H., Urakawa, S., Nakano, H., Small, R. J., Kim, W. M., Yeager, S. G.,
 967 ... Yamazaki, D. (2018). JRA-55 based surface dataset for driving
 968 ocean–sea-ice models (JRA55-do). *Ocean Modelling*, 130, 79–139. doi:
 969 10.1016/j.ocemod.2018.07.002
- 970 Turner, J. S. (1973). *Buoyancy effects in fluids*. Cambridge University Press. doi: 10
 971 .1017/CBO9780511608827
- 972 Turner, J. S. (1986). Turbulent entrainment: the development of the entrainment as-
 973 sumption, and its application to geophysical flows. *Journal of Fluid Mechanics*,

- 974 173, 431–471. doi: 10.1017/S0022112086001222
- 975 Umlauf, L., & Burchard, H. (2003). A generic length-scale equation for geophysical
 976 turbulence models. *Journal of Marine Research*, 61(2), 235–265. doi: 10.1357/
 977 002224003322005087
- 978 Umlauf, L., & Burchard, H. (2005). Second-order turbulence closure models for geo-
 979 physical boundary layers. A review of recent work. *Continental Shelf Research*,
 980 25(7-8), 795–827. doi: 10.1016/j.csr.2004.08.004
- 981 Ushijima, Y., & Yoshikawa, Y. (2020). Mixed layer deepening due to wind-induced
 982 shear-driven turbulence and scaling of the deepening rate in the stratified
 983 ocean. *Ocean Dynamics*, 70(4), 505–512. doi: 10.1007/s10236-020-01344-w
- 984 Van Der Laan, M. P., Kelly, M., Floors, R., & Peña, A. (2020). Rossby number
 985 similarity of an atmospheric RANS model using limited-length-scale turbu-
 986 lence closures extended to unstable stratification. *Wind Energy Science*, 5(1),
 987 355–374. doi: 10.5194/wes-5-355-2020
- 988 Van Roekel, L., Adcroft, A. J., Danabasoglu, G., Griffies, S. M., Kauffman, B.,
 989 Large, W., . . . Schmidt, M. (2018). The KPP Boundary Layer Scheme for
 990 the Ocean: Revisiting Its Formulation and Benchmarking One-Dimensional
 991 Simulations Relative to LES. *Journal of Advances in Modeling Earth Systems*,
 992 10(11), 2647–2685. doi: 10.1029/2018MS001336
- 993 Vreugdenhil, C. A., & Gayen, B. (2021). Ocean Convection. *Fluids*, 6(10), 360. doi:
 994 10.3390/fluids6100360
- 995 Wagner, G. L., Hillier, A., Constantinou, N. C., Silvestri, S., Souza, A., Burns, K.,
 996 . . . others (2023). Catke: a turbulent-kinetic-energy-based parameterization
 997 for ocean microturbulence with dynamic convective adjustment. *arXiv preprint*
 998 *arXiv:2306.13204*.
- 999 Weber, J. E. (1983). Steady wind- and wave-induced currents in the open ocean.
 1000 *Journal of Physical Oceanography*, 13(3), 524 - 530. doi: [https://doi.org/
 1001 10.1175/1520-0485\(1983\)013<0524:SWAWIC>2.0.CO;2](https://doi.org/10.1175/1520-0485(1983)013<0524:SWAWIC>2.0.CO;2)
- 1002 Wilcox, D. C. (1988). Reassessment of the scale-determining equation for advanced
 1003 turbulence models. *AIAA Journal*, 26(11), 1299–1310. doi: 10.2514/3.10041
- 1004 Willis, G., & Deardorff, J. (1974). A laboratory model of the unstable planetary
 1005 boundary layer. *Journal of Atmospheric Sciences*, 31(5), 1297–1307. doi: 10
 1006 .1175/1520-0469(1974)031<1297:ALMOTU>2.0.CO;2

- 1007 Wyngaard, J. C. (1973). On the surface-layer turbulence. In *Workshop on micrometeorology* (pp. 101–149).
1008
- 1009 Zeierman, S., & Wolfshtein, M. (1986). Turbulent time scale for turbulent-flow calculations. *AIAA Journal*, *24*(10), 1606–1610. doi: 10.2514/3.9490
1010
- 1011 Zheng, Z., Harcourt, R. R., & D’Asaro, E. A. (2021). Evaluating Monin–Obukhov
1012 Scaling in the Unstable Oceanic Surface Layer. *Journal of Physical Oceanography*, *51*(3), 911–930. doi: 10.1175/JPO-D-20-0201.1
1013
- 1014 Zhu, Y., Zhang, R.-H., & Sun, J. (2020). North Pacific Upper-Ocean Cold Temperature Biases in CMIP6 Simulations and the Role of Regional Vertical Mixing.
1015 *Journal of Climate*, *33*(17), 7523–7538. doi: 10.1175/JCLI-D-19-0654.1
1016